ACS OMEGA

Open Access

http://pubs.acs.org/journal/acsodf

Article

Analyzing Temperature Distribution, Mass Transport, and Cell Performance in PEM Fuel Cells with Emphasis on GDL Face Permeability and Thermal Contact Resistance Parameters

Binyamin Binyamin and Ocktaeck Lim*

Cite This: *ACS Omega* 2024, 9, 1516−1534

Read Online

ACCESS | Metrics & More | Article Recommendations

ABSTRACT: Temperature distribution, mass transport, and current density are crucial parameters to characterize the durability and output performance of proton exchange membrane fuel cell (PEMFC), which are affected by thermal contact resistance (TCR) and gas diffusion layer (GDL) face permeability within both cathode and anode GDL porous jumps. This study examined the effects of TCR and GDL face permeability on a single PEM fuel cell's temperature profiles, mass transport, and cell performance using a three-dimensional, nonisothermal computational model with an isotropic gas diffusion layer (GDL). This model calculates the ideal thermal contact resistance by comparing the expected plate-cathode electrode temperature difference to the numerical and experimental literature. The combined artificial neural network-genetic algorithm (ANN-GA) method is also applied to identify the optimum powers and their operating conditions in six cases. Theoretical findings demonstrate that TCR and suitable GDL face permeability must be considered to optimize the temperature distribution and cell efficiency. TCR and GDL face permeability lead to a 1.5 °C rise in maximum cell temperature at 0.4 V, with a "Λ" shape in temperature profiles. The TCR and GDL face permeability also significantly impacts electrode heat and mass transfer. Case 6 had 1.91, 6.58, and 8.72% higher velocity magnitudes, oxygen mass fractions, and cell performances than case 1, respectively. Besides, the combined ANN-GA method is suitable for predicting fuel cell performance and identifying operation parameters for optimum powers. Therefore, the findings can improve PEM fuel cell performance and give a reference for LT-PEMFC design.

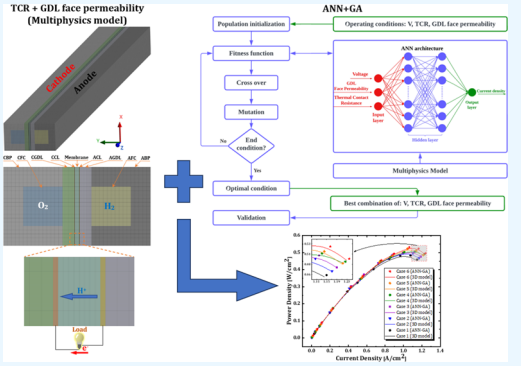

1. INTRODUCTION

The establishment of renewable energy resources is of utmost importance, primarily driven by the depletion of conventional energy sources and the environmental complexities associated with the utilization of fossil fuels. In recent years, there has been a global focus on the high power density and low emissions exhibited by proton exchange membrane (PEM) fuel cells. Unlike heat engines, PEM fuel cells instantaneously convert fuel chemical energy into electricity. Due to its freedom from the Carnot cycle, it can generate power at 40−60% efficiency.[1] PEMFC is harmless to the environment because it only generates heat and water. There are several applications for PEMFC, but the most popular ones are hybrid vehicles, portable power sources, and distributed power generation.[1−3] Developing a model to estimate total PEMFC performance is essential for commercialization.[4] After determining PEMFC performance, prior researchers can make targeted tweaks to increase performance in particular operational parameters.[5−7] On the other hand, one issue with standard modeling is that fuel cells have several physicochemical processes. To effectively use traditional fuel cell modeling techniques like analytical and mechanistic models, one must deeply understand the fuel cell process parameters and the underlying physical processes.[8]

The thermal contact resistance (TCR) between the bipolar plate (BP) and the gas diffusion layer (GDL) is often neglected in previous research.[6−9] Throughout the past few decades, numerous steady-state thermal models have been created, each capable of accurately reflecting static performance. Ge et al.[9] reported through modeling that the cathode catalyst layer (CCL) attained temperatures 12 °C higher than those in the flow channel. Energy transmission can occur in three main ways: by conduction due to a temperature difference, via convection due to the bulk movement of a fluid, or via diffusive transport in interdiffusion mixes. Numerical simulations have been the most popular method for researching heat transfer because of the benefits of collecting complete temperature field

Received: October 11, 2023
Revised: November 19, 2023
Accepted: December 5, 2023
Published: December 18, 2023

distributions for each component.[10−12] Cao et al.[13] examined this relationship using three-dimensional (3D) models. In the study, a voltage of 0.6 V predicted a current of 1.5 °C, which was 0.3 °C off. These basic models often disregard phase changes and the diffusion of heat and energy. PEMFC heat comes from electrode reactions (reversible and irreversible), Joule heating (powered by electron−proton conduction), and water phase change heat.

Moreover, PEMFCs in the automotive sector are complex systems due to the rapidly fluctuating loads in the application. Time to react, phase shift, heat conduction, and other parameters all play a role in determining the interior temperature.[13,14] Thus, transient models are more accurate when compared with steady-state thermal models. However, investigations on transient heat transmission are far fewer than those on steady-state heat transfer.[14,15] Two-dimensional (2D) models were designed by Burheim and Pollet,[16] who found that the inner temperature differential dropped significantly when wet. Wang et al.[17] designed a two-phase, three-dimensional transient model in which liquid water evaporation caused a "cold spot" at CCL. Besides that, they used a quasi-2D numerical model to investigate temperature changes throughout the PEMFC start-up procedure. Binyamin and Lim[18] studied tapered flow field configuration while considering TCR and PMT on temperature distribution and cell performance. The finding indicated that adding both suitable TCR and PMT on the tapered flow field model can improve cell performance by at least 12.63% compared with case 1 (original model).

In particular, the thermal contact resistance (TCR) between the collector rib and the GDL face permeability variation effect has typically been ignored in earlier research. On the other hand, some research has presented that contact resistance must not be disregarded. Internal temperature profile effects of anisotropic thermal conductivity and thermal contact conductance in a PEMFC were studied by Bapat and Thynell[19] using a two-dimensional single-phase model. They discovered that thermal contact conductance significantly impacted the temperature distribution within the PEMFC. In comparison, they looked at the thermal contact resistances of GDL and graphite at various compressive pressures. The bulk resistance of GDL is equal to its contact resistance with the graphite collector, as stated by Nitta et al.[20] According to the most up-to-date research on GDL's thermal contact resistance at different compressive pressures conducted by Sadeghi et al.,[21] thermal contact resistance is the most crucial factor in the material's overall thermal resistance.

According to Zhao et al.,[22−24] operating PEM fuel cells at an appropriate temperature is imperative. Their experimental verification showed that working the PEMFC at an unsuitable temperature results in a decline in performance and a reduction in the service life of the fuel cell. In a study conducted by Shang et al.,[25] it was empirically shown that the performance of a PEM fuel cell could be enhanced by utilizing a Nafion membrane modified with a complex of polymeric acid. This improvement was explicitly observed when the PEMFC was operated at an elevated temperature ranging from 333 to 353 K. In their experimental study, Liu et al.[26] observed a correlation between the operating temperature and the water content in the electrodes and membrane of a PEM fuel cell. They further noted that water content variations influenced the cell's impedance, thereby impacting the overall output performance of the PEMFC. Traditional three-dimensional simulations of PEM fuel cells do not consider the presence of thermal contact resistance (TCR).[27] These simulations assume that TCR does not influence the heat transfer between different components within the PEMFC. However, TCR is a significant factor in the thermal resistance of PEMFCs[28−30] and has a notable impact on the distribution of inner temperature and overall performance of the PEM fuel cell.

Xu et al.[31] studied staggered trapezoidal PEMFC flow channel baffles. The centerline of the gas diffusion layer-catalytic layer interface at the inlet had 1.7 mol m^{-3} oxygen, greater than the basic flow channel's 1.5. Results show that staggered trapezoidal baffles increase the net power density significantly. Top staggered trapezoidal baffles with height and depth of 0.825 and 0.126 mm increased the net power density by 8.92%. Xu et al.[32] examined how trapezoidal channel design and baffle adjustment affect PEM fuel cell net power density. The study used an upper side length of 1.234 mm, a lower side length of 1.8 mm, and a baffle 9.5 mm from the entry. This design increased the net power density by 4.347%. Pang and Wang[33] employed a CNN to analyze neutron radiography pictures to identify water spatial variation under different operational conditions and investigate fuel cell segment 5 and 10 spatial discrepancies. The results show that image preprocessing boosts convolution neural network accuracy to 96.6%. Liquid water appears 55% downstream for 50% relative humidity, while the entire cell experiences a two-phase flow for 100% humidity. Convolutional neural network results match pixelation image processing data with 91.8% accuracy. Other researchers, e.g., Wang et al.[34] optimized PEM fuel cell deformed GDLs utilizing multiphysics and machine learning surrogate modeling used response surface methodology (RSM) vs artificial neural network-based machine learning. Optimization of GDL is effective and efficient with M5. Current density and oxygen distribution standard deviation improved by 20.8 and 74.6% at 0.4 V. The Pareto front balances cell efficiency with oxygen distribution homogeneity. Saving 26.0% of the oxygen distribution standard deviation increases current density by 20.5%.

The findings from prior research investigations indicate that the thermal contact resistance substantially influences the operational temperature and output efficiency of PEM fuel cells. However, there is a lack of research investigating the combined impact of specific modifications in thermal contact resistance (TCR) and GDL face permeability on temperature profiles, mass transfer, and cell performance in PEM fuel cells. Hence, this study examines the impact of altering the GDL face permeability, and the thermal contact resistance is defined in six cases, as outlined in Table 2. This investigation employs a three-dimensional nonisothermal numerical model that encompasses the temperature profiles, mass transport, and performance aspects of a PEM fuel cell in a comprehensive manner. The numerical results, such as the polarization curve and temperature disparity between the cathode plate and electrode, are validated by comparing the experimental findings reported in the literature. Subsequent simulations are conducted by varying the TCR and GDL face permeability to analyze their impact on temperature distribution, mass transport, and the performance of PEM fuel cells.

2. NUMERICAL MODEL DEVELOPMENT

2.1. Assumption. A fuel cell is a complex device that operates by electrochemical processes, and several circumstances and surrounding activities influence its performance

https://doi.org/10.1021/acsomega.3c07932
ACS Omega 2024, 9, 1516−1534

and properties. A fuel cell is a complex apparatus involved in electrochemical reactions, whereby various circumstances and surrounding actions affect fuel cell performance and characteristics alteration. Multiple hypotheses have been formulated for the model to simplify the equation for the simulation analysis. These hypotheses are outlined as follows

1. The fuel cell operates in a steady-state arrangement.
2. Gases exhibit an incompressible flow behavior.
3. All gases are commonly regarded as ideal gases.
4. The flow of the fuel cell is characterized by laminar behavior.
5. The influence of gravity on the system is contra-*Y*-direction.
6. The textures in the membrane and GDL exhibit consistent porosity and isotropy.

2.2. Geometric Model. A three-dimensional computational model of a single-channel PEMFC is developed in this section. The SpaceClaim module creates the geometric model. The PEMFC topologies shown in Figure 1 are made up of five

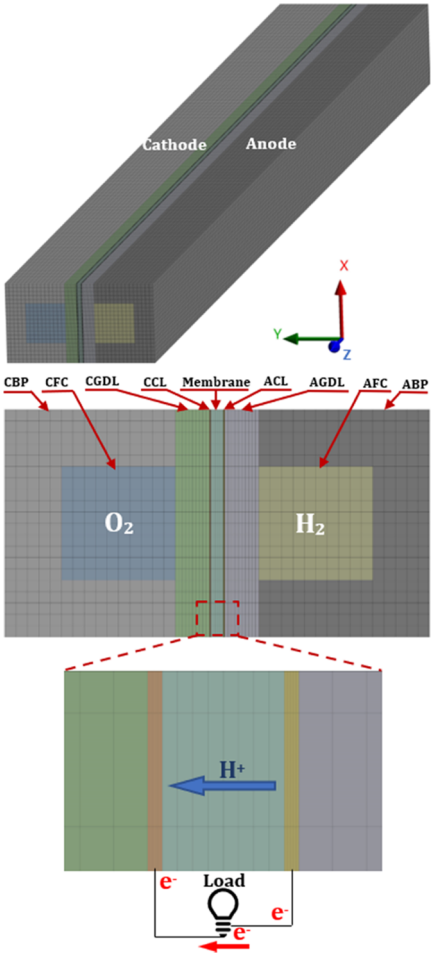

Figure 1. Diagram depicting the model geometry, structure, and computational domains of a single PEM fuel cell.

parts: A bipolar plate (current collector), flow channels, gas diffusion layers (GDLs), catalyst layers (CLs), and proton exchange membrane. The particular geometric parameters, as reported in Table 1, are compatible with the experiment instance of Wang et al.[35] This is the most prevalent PEMFC model. Because of its basic shape, the effort of computational

Table 1. Geometric Parameters for a Single Cell of PEMFC, Adapted from References 1,18

no.	parameters	value (mm)
1	channel height	1
2	channel width	1
3	width of rib	1
4	width of cell width	2
5	channel length	40
6	thickness of CL	0.0129
7	thickness of membrane	0.108
8	thickness of GDL	0.3

fluid dynamics (CFD) computation may be decreased, allowing the task to focus primarily on the use and/or lack of thermal contact resistance modeling.[36] After successfully using the SIMPLE solver to this basic model, it may be adapted to other more sophisticated and complicated PEMFC models; more detail of the numerical solution can be seen in Figure 2. The anode flow channel of a PEM fuel cell is continually supplied with hydrogen. Hydrogen is broken into positive protons and negative electrons at the CL after passing through the GDL. Electrons pass through an external circuit to the corresponding load, whereas positive hydrogen protons

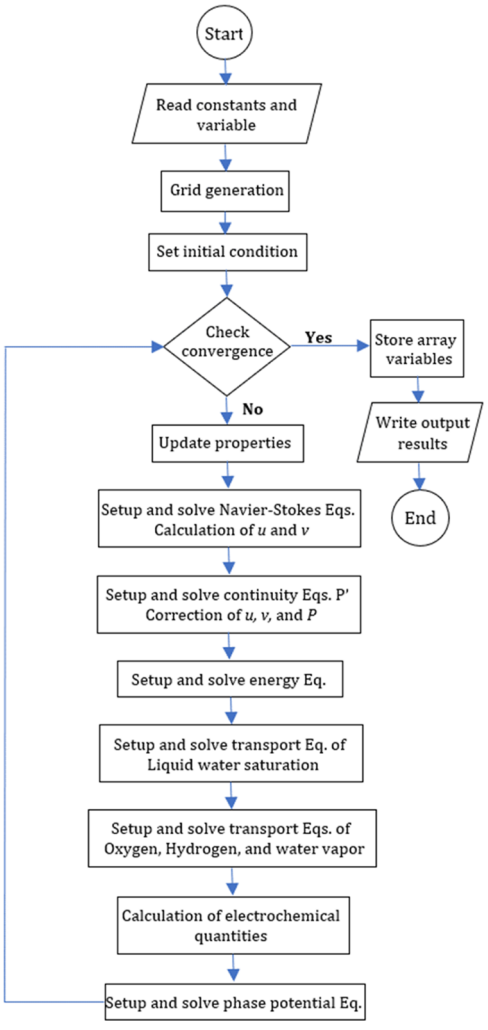

Figure 2. Algorithm of computational solution.

https://doi.org/10.1021/acsomega.3c07932
ACS Omega 2024, 9, 1516−1534

diffuse across the membrane to the cathode.[1] Electrical current is created as a result of the preceding operation.

The description cases used to calculate the GDL face permeability and TCR between BPs and GDLS are presented in Table 2. The authors apply this to all of the simulated cases regarding the various GDL face permeability and TCR on the PEM fuel cell.

Table 2. Description of the Simulated Cases Regarding the Various GDL Face Permeabilities and TCR

case no.	GDL face permeability (m^{-2})	TCR (m^2·KW)
1	1.76×10^{11}	0
2	1.50×10^{12}	1.00×10^{-04}
3	2.25×10^{12}	2.50×10^{-03}
4	2.50×10^{12}	5.00×10^{-03}
5	3.25×10^{12}	7.50×10^{-02}
6	3.50×10^{12}	1.00×10^{-01}

2.3. Conservation Equations. This section briefly describes the computational model applied in this investigation. The foundation of our current model is a two-phase model that has been adapted from the literature[22,23] to include isotropic transport mechanisms in gas diffusion layers. It is considered that the cell is in a steady state. It is expected that the gas mixing of the reacting gas is ideal. The assumption of a laminar flow in the gas is made. Since the gas channel is moving at a relatively high velocity, it is hypothesized that liquid saturation in the flow channel is mostly negligible.

The following expression demonstrates how a standard convection-diffusion equation can be used to express the conservation of energy, mass, momentum, species, and charges.

$$\nabla\cdot(\tilde{\rho}U\phi) = \nabla\cdot(\Gamma_\phi\nabla\phi) + S_\phi \tag{1}$$

where ϕ is the general variable to be found out, Γ_ϕ is the generalized diffusion coefficient of ϕ, S_ϕ is the variable's source term ϕ, and $\tilde{\rho}$ is the nominal density. Table 3 lists the expressions of ϕ, $\tilde{\rho}$, and Γ_ϕ for some expressions.

Table 3. ϕ, $\tilde{\rho}$, and $\Gamma_\varnothing$ of Various Governing Equations, Adapted from Reference 13

	energy	mass	momentum	species	charges
ϕ	T	1	U	Y_i	φ_s, φ_{mem}
$\tilde{\rho}$	ρ_{mix}	ρ_{mix}	$\rho_{mix}/\varepsilon_{eff}^2$	ρ_{mix}	0
$\Gamma_\varnothing$	λ_{eff}/C_p	0	$\mu_{mix}/\varepsilon_{eff}$	$\rho_{mix}\, D_i^{eff}$	σ_{sol}, σ_{mem}

Moreover, an equation for the transfer of liquid water through a porous electrode can be stated as

$$\nabla\cdot\left(\rho_l\frac{\eta_g}{\eta_l}\frac{\kappa_{rl}}{\kappa_{rg}}u_g\right) = \nabla\cdot(\rho_l D_c\nabla S) - S_l \tag{2}$$

where D_c is the diffusivity of s, and S_l is the saturation of liquid water, which is linked to capillary pressure as

$$D_c = -\frac{KK_l}{\eta_l}\frac{dp_c}{ds} \tag{3}$$

The expression for the movement of dissolved water through a membrane is as follows

$$\nabla\cdot(D_w\nabla C_w) - \nabla\cdot\left(n_d\frac{i}{F}\right) = \mathbf{S}_d \tag{4}$$

where D_w is the diffusion coefficient, n_d is the electro-osmotic drag coefficient, and C_w is the water content in the membrane phase.

2.4. Boundary Condition and Computational Method. There is a mass flow inlet condition at the channel's inlet and a pressure outlet situation at the outlet. We can use the following formula to get the inlet velocities[1]

$$u_a^{in} = \zeta_a\frac{i_{max}}{2F}A_{MEA}\frac{1}{\omega_{H_2}^{in}}\frac{RT_a^{in}}{p_a^{in}}\frac{1}{A_{ch}} \tag{5}$$

$$u_c^{in} = \zeta_c\frac{i_{max}}{4F}A_{MEA}\frac{1}{\omega_{O_2}^{in}}\frac{RT_c^{in}}{p_c^{in}}\frac{1}{A_{ch}} \tag{6}$$

where ζ is the ratio of stoichiometric, R is the gas constant (8.314 J mol^{-1} K^{-1}), F is the Faraday constant (96,487 °C mol^{-1}), and i_{max} is the maximum average current density. The geometrical area of the MEA is denoted by the notation A_{MEA}, while A_{ch} denotes the cross-sectional area of the channel. T is the intake temperature, and p is the inlet pressure. It is the mass fraction of the inlet species, all of which may be determined from the inlet conditions of the temperature, relative humidity, and pressure. In addition to the input velocity, the mass fraction and temperature of the gas mixture are provided at the input boundary as follows

$$Y_{H_2} = Y_{H_2,in},\ Y_{O_2} = Y_{O_2,in},\ Y_{H_2O} = Y_{H_2O,in},\ T_{in} = T_{cell} \tag{7}$$

where $Y_{H_2,in}$, $Y_{O_2,in}$, and $Y_{H_2O,in}$ are readily calculable from the molar fraction, and the water vapor molar fraction, X_{H_2O}, can be estimated from the humidity of the gas entering the system as

$$X_{H_2O},\ a = \frac{RH_aP_{sat}}{P_a},\ X_{H_2O},\ c = \frac{RH_cP_{sat}}{P_c} \tag{8}$$

The oxygen molar fraction, X_{O_2}, and hydrogen molar fraction, X_{H_2}, are then calculated since just elemental hydrogen and oxygen are used.

$$X_{H_2} = 1 - X_{H_2O,a},\ X_{O_2} = 1 - X_{H_2O,c} \tag{9}$$

The completely developed assumption is employed at the outlet border, where the gas is released.[38]

$$\frac{\partial\phi}{\partial X} = 0 \tag{10}$$

Anode and cathode outer surface: Transmission of electrons between the anode and cathode occurs via the outer circuit, as depicted in Figure 1. The electronic potential and temperature are set in step one.

$$\varphi_{s,a} = 0,\ \varphi_{s,c} = V_{cell},\ T = T_w = T_{cell} \tag{11}$$

Using the adiabatic assumption for the proton potential

$$\frac{\partial\varphi_m}{\partial Z} = 0 \tag{12}$$

Periodical boundary line in the y-axis: Since the structure is periodic in the y-axis, the symmetry condition is adapted to the surface in the outer y-axis.

https://doi.org/10.1021/acsomega.3c07932
ACS Omega 2024, 9, 1516−1534

Table 4. Complementary Expression and Corresponding Definitions

parameters	expressions
coefficient of GDL effective mass diffusion[26,27]	$D_{\text{eff}} = f(\varepsilon)D_{i,\text{bulk}}$, $D_{i,\text{bulk}} = D_i^0\left(p_0/p\right)^{1.0}(T/T_0)^{1.5}$
	through plane: $f(\varepsilon)_{\text{th}} = 1 - 2.76\varepsilon\cosh(3\varepsilon - 1.92)[3(1-\varepsilon)/(3-\varepsilon)]$
	in-plane: $f(\varepsilon)_{\text{in}} = 1 - 1.72\varepsilon\cosh(2.07\varepsilon - 2.11)[3(1-\varepsilon)/(3-\varepsilon)]$
over-potential	$\eta_a = \phi_s - \phi_m, \eta_c = V_{oc} - \phi_s + \phi_m$
open circuit voltage[37]	$V_{oc} = 1.23 - 0.9\times10^{-3} + 2.3\frac{RT}{4F}\log(p_a^2 p_c)$
water saturation pressure[37]	$\log_{10}P_{\text{sat}} = -2.1794 + 0.02953T - 9.1837\times10^{-5}T^2 + 1.4454\times10^{-7}T^3$
relative permeability[37]	$K_{rl} = S^3$, $K_{rg} = (1-S)^3$
GDL Intrinsic permeability[41]	$\frac{K}{R^2} = \frac{\varepsilon(\varepsilon-\varepsilon_p)^{\alpha+2}}{8(\ln\varepsilon)^2(1-\varepsilon)^{\alpha}[(\alpha+1)\varepsilon-\varepsilon_p]^2}$
effective thermal conductivity of GDL[42]	through plane: $k_{\text{eff}}^{\text{th}}/k_s = 1 - 0.963(1-\varepsilon)^{-0.008}\exp[0.881(1-\varepsilon)]$ $[3\varepsilon/(3-(1-\varepsilon))]$
	in-plane: $k_{\text{eff}}^{\text{th}}/k_s = 1 - 0.977(1-\varepsilon)^{-0.009}\exp[0.344(1-\varepsilon)]$ $[3\varepsilon/(3-(1-\varepsilon))]$
electrochemical kinetics[37−383940414243]	$R_a = \theta A_s i_{a,\text{ref}}\left(\frac{C_h}{C_{h,\text{ref}}}\right)^{1/2}\left\{\exp\left[\frac{\alpha_a F}{RT}\eta_a\right] - \exp\left[-\frac{(1-\alpha_a)F}{RT}\eta_a\right]\right\}$
	$R_c = \theta A_s i_{c,\text{ref}}\frac{C_o}{C_{o,\text{ref}}}\left\{\exp\left[\frac{\alpha_c F}{RT}\eta_c\right] - \exp\left[-\frac{(1-\alpha_c)F}{RT}\eta_c\right]\right\}$
membrane electrical conductivity[44]	$\sigma_{\text{mem}} = (0.5193\lambda - 0.326)\exp\left[1268\left(\frac{1}{303} - \frac{1}{T}\right)\right]$
effective electrical conductivity of GDL[44]	through plane: $\sigma_{\text{eff}}^{\text{th}}/k_s = 1 - 0.962(1-\varepsilon)^{-0.007}\exp[0.889(1-\varepsilon)]$ $[3\varepsilon/(3-(1-\varepsilon))]$
	in-plane: $\sigma_{\text{eff}}^{\text{th}}/\sigma_s = 1 - 0.962(1-\varepsilon)^{-0.016}\exp[0.367(1-\varepsilon)]$ $[3\varepsilon/(3-(1-\varepsilon))]$
capillary pressure[45]	$p_c = \left(\frac{\varepsilon}{K}\right)^{0.5}\sigma J(s)$, $J(s) = \begin{cases}\cos\theta_c[1.417(1-s) - 2.212(1-s)^2 + 1.236(1-s)^3]\ \theta_c < 90^\circ \\ \cos\theta_c[1.417s - 2.212s^2 + 1.236s^3]\ \theta_c > 90^\circ\end{cases}$
membrane water diffusion coefficient[44]	$D_w = 2.1\times10^{-7}\exp(-2346/T)C_w$
electro-osmotic drag coefficient[46]	$n_d = \frac{2.5\lambda}{22}$
equilibrium membrane water content[46]	$\lambda_e = \begin{cases}1.41 + 22.3a_{H_2O} - 18.8a_{H_2O}^2 - 16.2a_{H_2O}^3, 0 \le a_{H_2O} \le 1 \\ 10.1 + 2.94(a_{H_2O} - 1) 1 < a_{H_2O} \le 3\end{cases}$
wate vapor activity[46]	$a_{H_2O} = \frac{x_w p}{p_{\text{sat}}} + 2s$

$$v = 0,\ \frac{\partial u}{\partial y} = 0,\ \frac{\partial W}{\partial y} = 0,\ \frac{\partial \phi}{\partial y} = 0 \tag{13}$$

Complementary equations related to coefficients of diffusivity or other empirical characteristics are needed to solve these governing equations correctly; these equations are listed in Table 4. Table 5 presents the equations that are used to determine the source term in each of the different regions.

2.5. Grid-Independent Verification and Model Validation. In order to address the aforementioned issue, a proprietary computer algorithm utilizing the finite volume method is employed. A hexahedral grid is chosen for the Z direction due to the significant variation in thickness among the different layers. In contrast, uniform grids are used for the X and Y directions, as depicted in Figure 1. The present model is based upon a two-phase concept that effectively encompasses isotropic transport phenomena occurring within gas diffusion layers. The cell is believed to stay at a consistent temperature and pressure throughout the experiment. The gas flow within the cell is characterized by a laminar pattern, indicating a smooth and orderly movement. The mixing of reactive gases is considered to be ideal, meaning that they combine in a perfectly homogeneous manner.

Additionally, the presence of liquid saturation in the gas channel is ignored due to the high velocity of the flow, which prevents significant liquid accumulation. The grid independence test employs five different grid systems as alternatives. The findings presented in Figure 3a indicate that the quantities of the five grids are 496,000, 512,000, 544,000, 560,000, and 592,000, respectively. In this study, the grid system considers the balance between precision and economics, resulting in a more stable value of the current densities. The number of grids in this work corresponds to 544,000 for the best choice. It is often postulated that the solid walls possess negligible flux and

https://doi.org/10.1021/acsomega.3c07932
ACS Omega 2024, 9, 1516−1534

Table 5. Equation of State for Source Term in Various Regions, Adapted from Reference 47

equation	source terms
mass	in GDL: $S_m = S_h + S_0 + S_w$
	in CL: $S_m = S_t$
momentum	in GDL: CL: $S_u = -\frac{\mu_g \mathbf{u}_g}{KK_{rg}} - \nabla p_g$
	in GC: $S_u = -\nabla p_g$
species	in ACL: $S_h = -\left(\frac{R_a}{2F}\right)M_h$
	in CCL: $S_O = -\left(\frac{R_c}{2F}\right)M_O$
potential	in CL: $S_w = -\left(\frac{R_c}{2F}\right)M_w + S_d + S_l$
	in GDL: $S_w = S_l$
	in ACL: $S_{\phi,s} = -R_a$
	in CCL: $S_{\phi,s} = -R_c$
energy	in CL: $S_T = i\left(\eta + T\frac{dE}{dT}\right) + \frac{I^2}{\sigma_s} + S_l h_{fg}$
	in GDL: $S_T = \frac{I^2}{\sigma_s} + S_l h_{fg}$
	in MEM: $S_T = \frac{I^2}{\sigma_{mem}}$
liquid saturation	in CL: GDL: $S_l = A_{pore}\frac{Sh_c D_w}{d}(1-s)(\rho_w - \rho_{sat})q + A_{pore}\frac{Sh_c D_w}{d}s(\rho_w - \rho_{sat})(1-q)$
dissolved water	in ACL: $S_{d,a} = -\gamma_a(C_{w,a} - a^*_{w,a})$
	in CCL: $S_{d,c} = -\gamma_d(C_{w,c} - a^*_{w,c}) + R_c/2F$

exhibit no sliding. The anode terminal is configured to have zero voltage at its wall. At the cathode terminal wall, there is a voltage variation of 0.05 V within the range of 0.90 to 0.40 V. The SIMPLE technique is commonly employed for pressure–velocity coupling, whereas the interpolation functions are implemented using the second-order upwind approach. The energy equation is considered converged when the residual falls below a threshold of 10×10^{-6}, whereas the remaining equations are deemed converged when their residuals reach a threshold of 10×10^{-3}. Table 6 provides a concise overview of the operating procedures employed for numerical validation, drawing from a comprehensive analysis of relevant literature.[35]

Table 6. Operating Parameters for Validation, Adapted from Reference 1

no.	parameters	value
1	open-circuit voltage	0.95 V
2	operating temperature	70 °C
3	operating pressure	1 atm
4	reference current density for cathode	5210 A m^{-2}
5	reference current density for anode	9×10^8 A m^{-2}
6	relative humidity of inlet gases	100%
7	GDL porosity	0.4
8	CL porosity	0.5
9	membrane porosity	0.25
10	H_2 reference concentration	54.7 mol m^{-3}
11	O_2 reference concentration	3.39 mol m^{-3}
12	ratio of anode stoichiometric	3
13	ratio of cathode stoichiometric	3
14	anode concentration exponent	0.5
15	cathode concentration exponent	1
16	H_2 reference diffusivity	3.9×10^{-5} m^2 s^{-1}
17	O_2 reference diffusivity	2.275×10^{-5} m^2 s^{-1}
18	H_2O reference diffusivity	3.9×10^{-5} m^2 s^{-1}
19	other species reference diffusivity	5.2×10^{-5} m^2 s^{-1}
20	anode fuel	H_2 (20%) and H_2O (80%)
21	cathode fuel	O_2 (18.5%) and H_2O (22%)

The polarization curves generated by the computational multiphysics model are compared to both simulated and experimental data from Li et al.[1] and Wang et al.,[35] respectively, to ensure reliability. This comparison is illustrated in Figure 3b. The models are evaluated within four distinct experimental conditions, each characterized by unique combinations of temperatures and pressures. Supplementary operational elements employed in generating the polarization curves are presented in Table 6. The validation of the model involves assessing the conformity of the three polarization curves obtained under different operating settings, with the

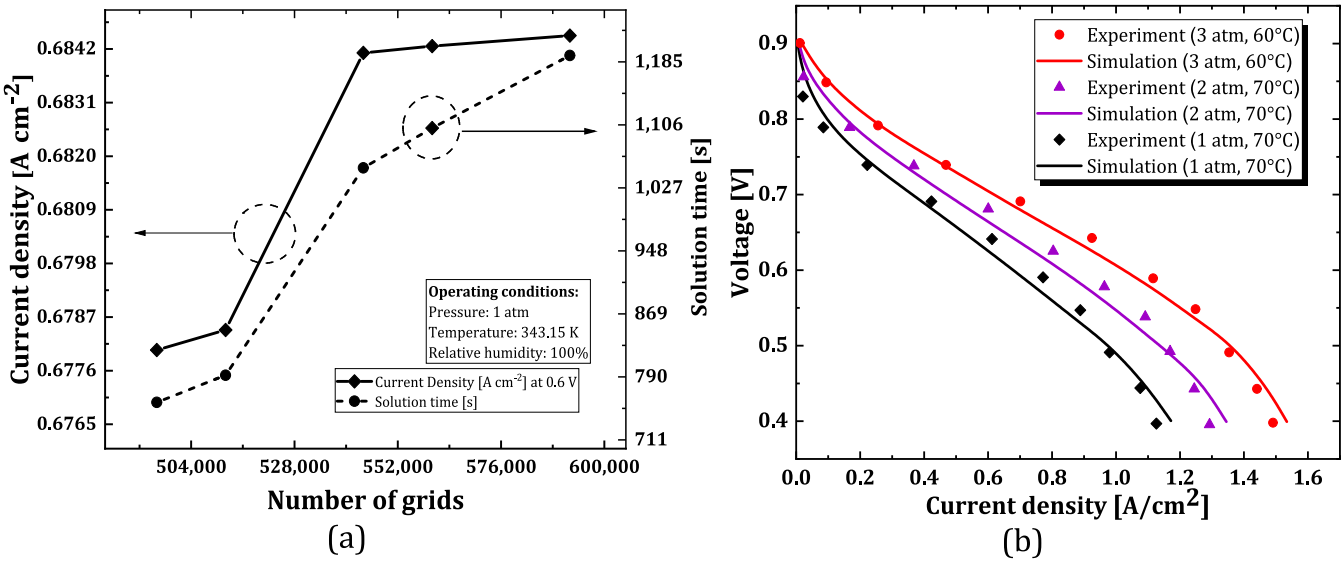

Figure 3. (a) Verification of grid independence for the current density at a voltage of 0.60 V. (b) Comparison of polarization curves between the PEMFC simulation and the experimental one for a straight channel.

https://doi.org/10.1021/acsomega.3c07932
ACS Omega 2024, 9, 1516−1534

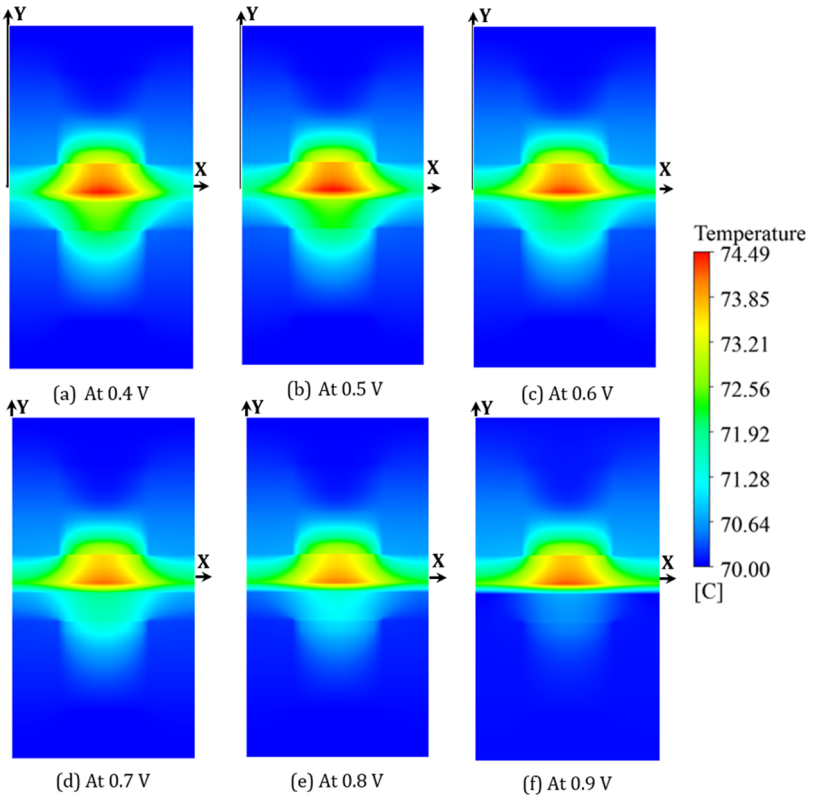

Figure 4. Temperature variations on XY plane (40 mm from origin of *Z*-axis) at various cell voltages without considering TCR (operating pressure, P = 1 atm; operating temperature, T = 70 °C; cathode gas: oxygen; anode gas: hydrogen).

experimental findings ensuring their acceptability. Significantly, the model demonstrates superior performance compared to the tests under conditions of elevated current density. The reason for this is that the CFD analysis[48] was based on a single-phase model, which is limited in its ability to accurately predict the performance of PEM fuel cells at high current densities. Furthermore, it is essential to consider other elements that can contribute to these phenomena, including compressive forces,[49] an uneven temperature and pressure distribution, and the limitations imposed by the single-cell model.[1]

3. RESULTS AND DISCUSSION

This section presents an in-depth investigation of the computational results pertaining to the PEM fuel cell's temperature distribution, cell performance, and mass transport characteristics under various conditions. First, we will discuss the impact of the GDL face permeability and thermal conductivity ratio (TCR) between the collector rib and the gas diffusion layer (GDL) on the heat transfer process. Table 2 provides a comprehensive summary of all simulated instances pertaining to the influence of GDL face permeability and thermal contact resistance on the temperature profile, mass transfer, and performance. This study examines the impact of variations in porous medium thickness and thermal contact resistance on temperature distributions and cell performance. This paragraph provides an elucidation of the temperature profile in different scenarios of heat dissipation.

3.1. Effect of TCR and GDL Face Permeability on Temperature Profiles. It is possible that the temperature of the PEM fuel cell will not always be set to the best conditions during actual operation. This may be the case due to restrictions in thermal management or specific operational operations, such as beginning. The rise in the temperature from room temperature to the point at which a fuel cell can function most efficiently is an illustration of an ignition process. The temperature of a tiny fuel cell that does not have an active thermal management component is determined mainly by the temperature of its surrounding environment, as well as its rate of waste creation. Because temperature plays such a vital role in the operation of fuel cells, it is essential for practical fuel cell control and system design to understand the maximum power that can be achieved at various temperatures. Both the temperature dependency of the maximum power and the determination of appropriate operating conditions have to be investigated.

Thermal contact resistance and GDL face permeability are present at the interface between the contact surfaces of different components within a functioning PEM fuel cell (PEMFC). The prevailing belief is that the contact resistance between the cathode catalyst layer (CCL) and the gas diffusion layer (GDL) is often considered negligible due to the utilization of a hot press method during the preparation of the membrane electrode assembly (MEA). However, the authors evaluate only the GDL face permeability and thermal contact resistance between the gas diffusion layer (GDL) and the collector. Based on the findings of Nitta et al.,[20] the thermal contact resistance between the graphite collector and the gas diffusion layer (GDL) exhibits variability ranging from 0.3×10^{-4} and 2.5×10^{-4} m^2 KW^{-1}, contingent upon the compression pressure applied. According to the findings of Sadeghifar et al.,[50] the thermal contact resistance between the BP and the GDL varies between 1.0×10^{-4} and 8.0×10^{-4} m^2 KW^{-1}, contingent upon the specific type of GDL utilized and the degree of compression exerted.

https://doi.org/10.1021/acsomega.3c07932
ACS Omega 2024, 9, 1516−1534

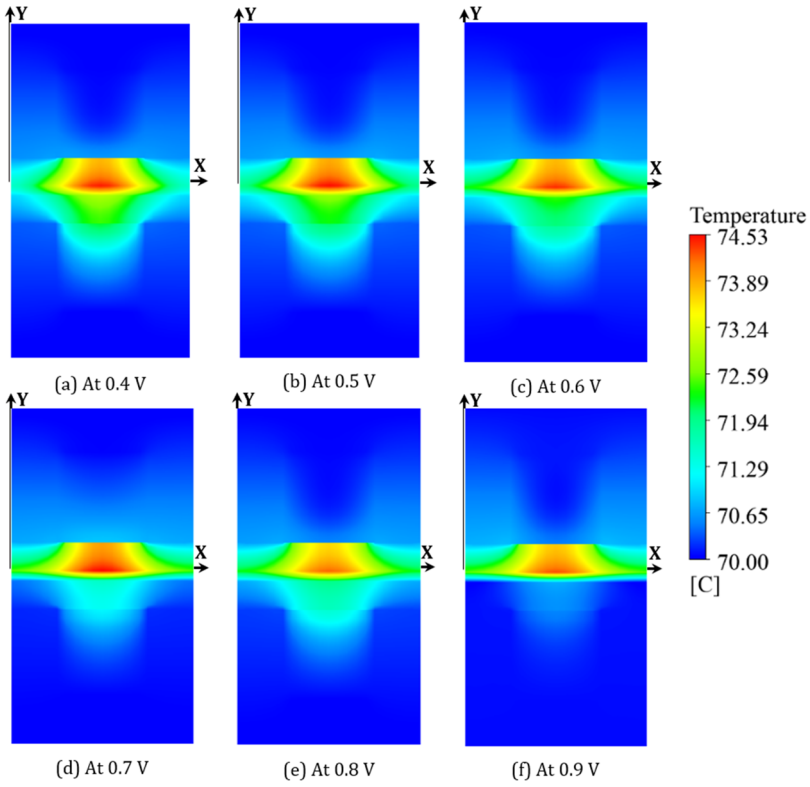

Figure 5. Temperature variations on *XY* plane (40 mm from origin of *Z*-axis) at various cell voltages with considering TCR (1.00×10^{-01} m^2·K/W) and GDL face permeability (3.50E12 m^{-2}) (operating pressure, P = 1 atm; operating temperature, T = 70 °C; cathode gas: oxygen; anode gas: hydrogen).

This study shows that the GDL face permeability and the TCR between the current collector and GDL range from 1.76 × 11 to 3.50 × 12 m^{-2} and 0 to 1.00×10^{-01} m^2 KW^{-1}, respectively (more detail, see Table 2). Figure 4 shows the temperature distributions without and Figure 5 with porous medium thickness and thermal contact resistances for output voltages ranging from 0.4 to 0.9 V. There is a temperature gradient between the current collector (rib) and channel regions, with the rib being cooler and the channel being hotter as one moves farther from it. Since the velocity in porous GDL is so low, we may infer that the rib region is responsible for conducting most of the heat dissipated by the electrode. Furthermore, it has been discovered that as TCR and GDL face permeability values increase, so does the optimum cell temperature. This is due to the fact that the presence of GDL face permeability and TCR between the collector rib and the GDL increases heat transfer resistance and makes heat dissipation within the porous electrode more complex. In addition to this, it is because both the GDL face permeability and the TCR prevent heat dissipation.

Figure 4 shows temperature profiles without considering the GDL face permeability and the TCR at the *XY* plane through the *Y*-axis direction. The most significant temperature is revealed to be located around the cathode catalyst layer because the oxygen reduction process generates the majority of the heat; when the output cell voltage lowers, the heat created in the cell rises, increasing the maximum temperature. Comparing Figure 5 reveals the impact of the GDL face permeability and TCR on the temperature profile within the PEMFC. The flow of current through the electrolyte membrane and the electrodes causes resistance, resulting in ohmic heating. This can lead to temperature variation within the MEA, with higher temperatures typically observed near areas of higher current density. Besides, the heat generated within the MEA must be transported and dissipated effectively to maintain a balanced temperature distribution. Variations in heat transfer rates and cooling mechanisms across the MEA can lead to temperature variations. Factors such as the thermal contact resistances and the porous medium thickness of the materials involved can affect heat dissipation. To begin with, disregarding the TCR and GDL face permeability can lead to underestimating the MEA's total temperature. The temperature results without GDL face permeability and the TCR are demonstrably lower than the temperature results with considering GDL face permeability and TCR; for instance, the optimum gradient temperature between these two cases is approximately 1.5 °C when the output cell voltage equals 0.4 V, and the average of temperature rising is 0.5 °C from all cell voltages condition.

Moreover, temperature distribution at iso-volume with various cell voltages (0.4−0.9 V) is depicted in Figure 6 without considering TCR and GDL face permeability. The maximum temperature is mainly generated from the middle of MEA with the highest temperature at 0.4 V cell voltage and the lowest temperature at 0.9 V cell voltage. Figure 7 shows that the polarization curve and power density correspond to the current density in six various cases with specific operating conditions. It is evident that the power density and current density increase as of case number, which the increase in the number of GDL face permeability and TCR have reliable results with recent literature.[13] The temperature patterns within the MEA differ in Figure 8a,b. The temperature patterns within MEA appear to be a "Λ" shape in Figure 8a,b. All of the motion mentioned above phenomena are entirely caused by

https://doi.org/10.1021/acsomega.3c07932
ACS Omega 2024, 9, 1516−1534

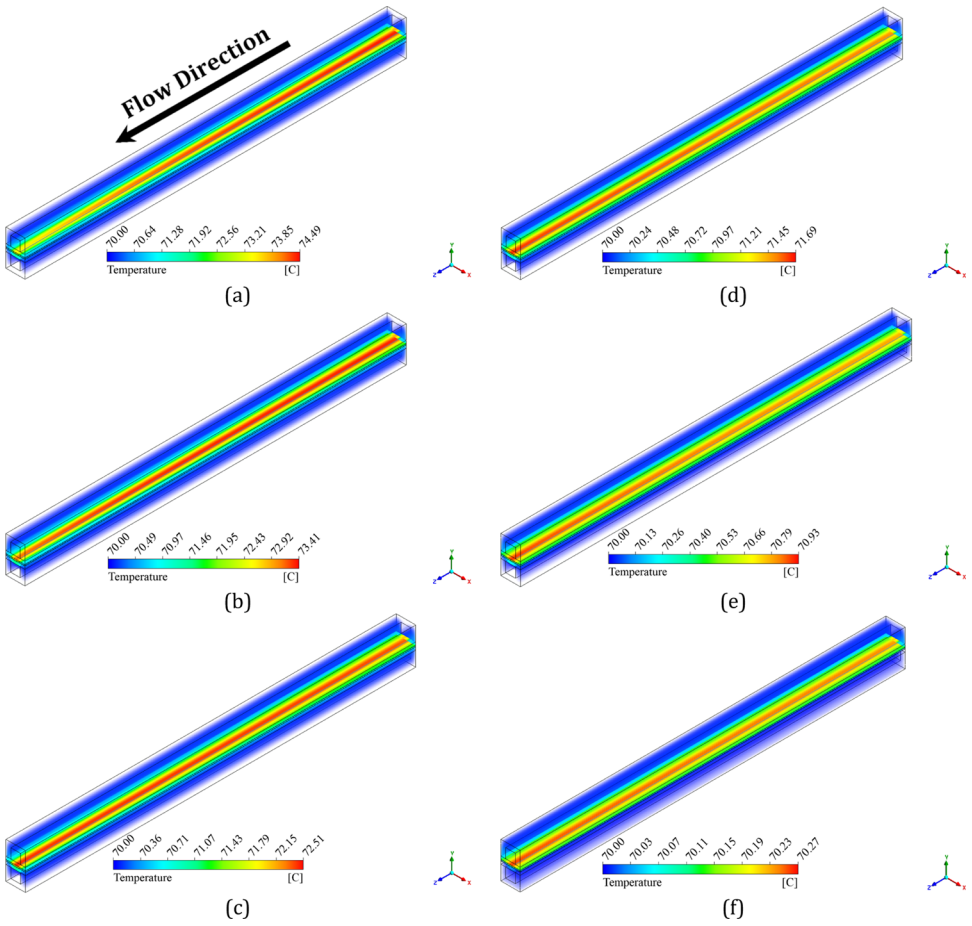

Figure 6. Distributions of temperature at iso view with various cell voltages: (a) 0.4 V, (b) 0.5 V, (c) 0.6 V, (d) 0.7 V, (e) 0.8 V, and (f) 0.9 V ignoring TCR (operating pressure, P = 1 atm; operating temperature, T = 70 °C; cathode gas: oxygen; anode gas: hydrogen).

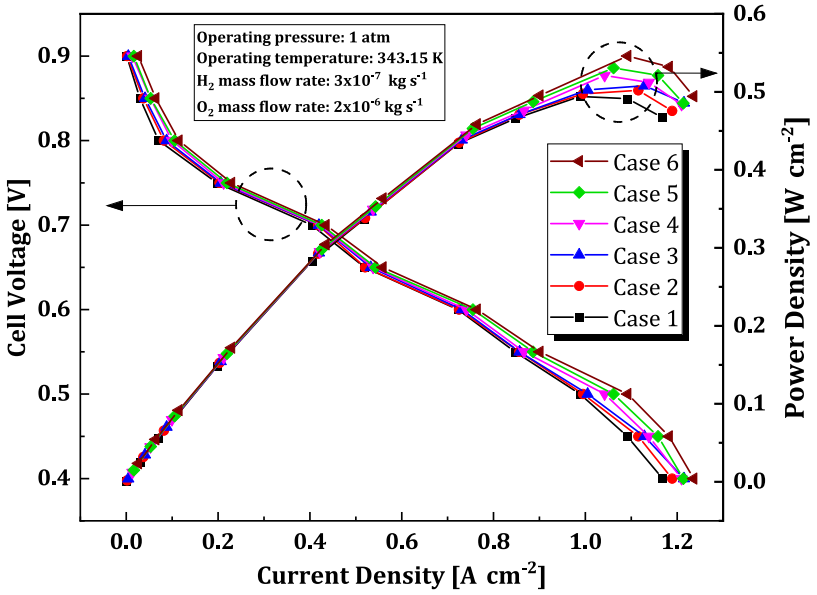

Figure 7. Current and power densities of various cases (operating pressure = 1 atm; operating temperature, T = 70 °C, O_2 mass flow rate: 2×10^{-6} kg·s^{-1}, H_2 mass flow rate: 3×10^{-7} kg·s^{-1}).

the TCR and the GDL face permeability between the current collector (rib) and GDL. In other words, the GDL face permeability and TCR between the BP and the GDL prevent heat dissipation, causing the MEA temperature increase, which is in line with the preceding study conducted by Cao et al.[13] As can be shown in Figure 8, the porous electrode heats more in TCR and GDL face permeability scenarios. Because the water saturation pressure rises with increasing electrode temperature,

https://doi.org/10.1021/acsomega.3c07932
ACS Omega 2024, 9, 1516−1534

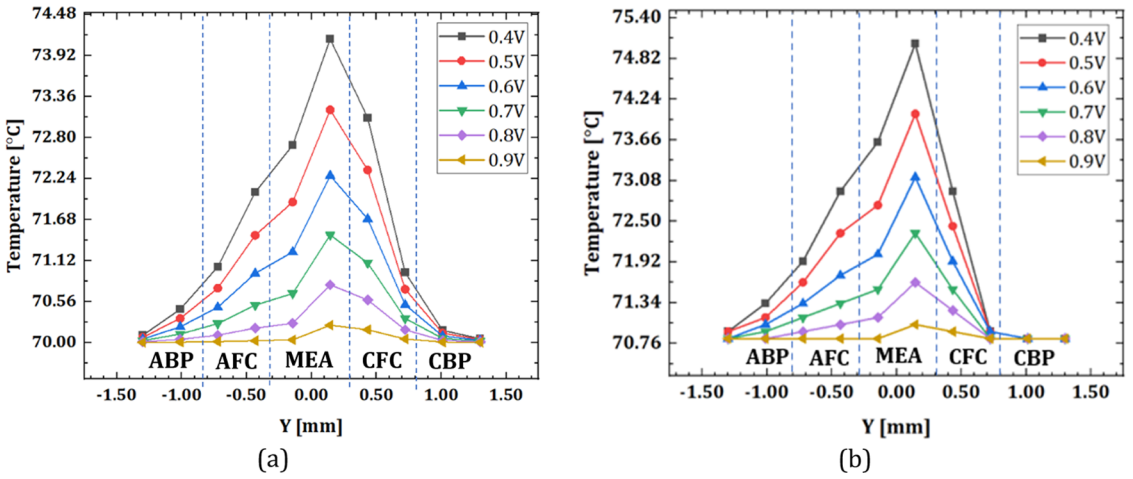

Figure 8. Profiles of temperature toward *Y*-axis with various cell output voltages: (a) without and (b) with TCR (1.00×10^{-01} m^2 K/W).

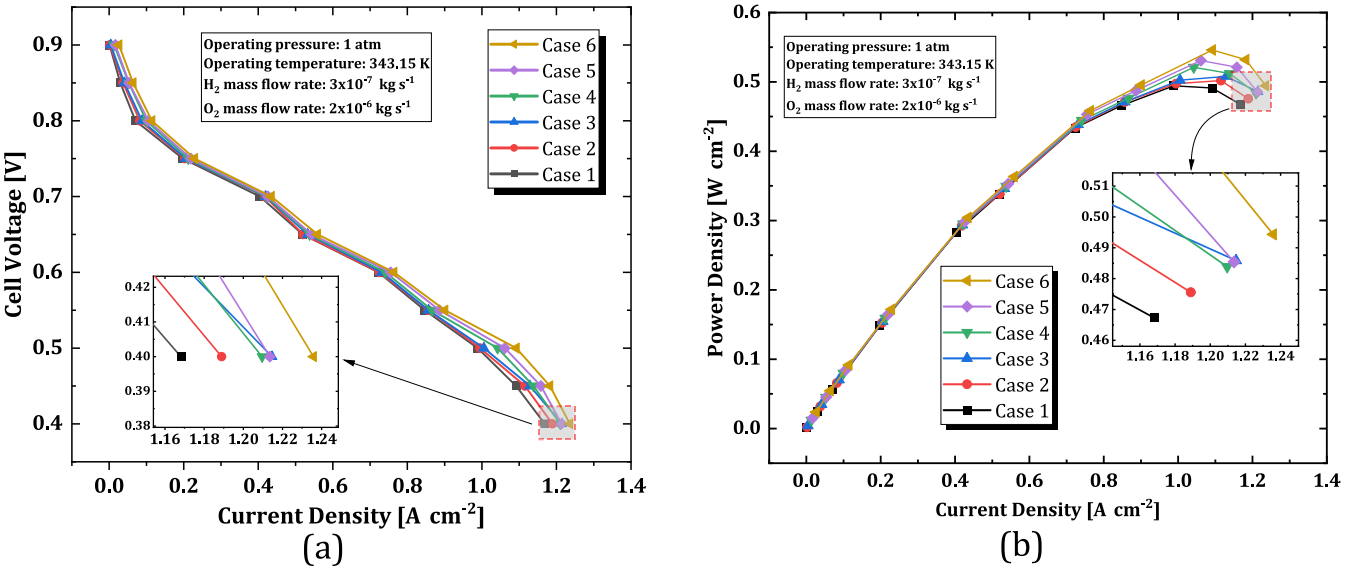

Figure 9. (a) Current density and (b) power density curves with different cases (operating pressure = 1 atm; operating temperature, T = 70 °C, O_2 mass flow rate: 2×10^{-6} kg s^{-1}, H_2 mass flow rate: 3×10^{-7} kg s^{-1}).

less water vapor condenses into liquid form. The reduced saturation in TCR and GDL face permeability can be attributed to this. At the same time, the electrochemical process and oxygen delivery by GDL to the reaction sites are enhanced by a rising temperature; likewise, decreasing the liquid water saturation in the GDL face permeability and TCR circumstances also aids in the transport of oxygen. Under these conditions, cell performance in GDL face permeability and TCR assays is much improved.

Figure 9a depicts the simulation outcomes of the 3D multiphysics model, specifically illustrating the polarization curve. Additionally, Figure 9b showcases the power density curves for six distinct scenarios, each characterized by different characteristics. Figure 9a illustrates that there is a minimal disparity in the current density among various scenarios beyond the threshold of 1.15 A cm^{-2}. As the operational voltages decline, the discrepancies in current density among various scenarios exhibit a progressive increase. The minimum current density, measuring 1.168 A cm^{-2}, is observed in case 1 when compared with all other cases. In contrast, example 6 demonstrates the greatest current density, with a measurement of 1.236 A cm^{-2}. This value surpasses that of case 1 by 0.068 A cm^{-2}, representing a relative increase of 6.8% at a voltage of 0.4 V. In addition, Figure 9b depicts the power density curve for six distinct cases. The data presented illustrate that the smallest peak power density observed in case 1 is 0.494 W cm^{-2}. However, the maximum peak power density recorded in case 6 is 0.546 W cm^{-2}, indicating a difference of 0.052 W cm^{-2} (equivalent to an 8.72% increase compared to case 1). This suggests that considering both the GDL face permeability and the thermal contact resistance (TCR) between the gas diffusion layer and the current collector can lead to improved PEM fuel cell performance.

3.2. Implementation of Artificial Neural Network (ANN) and Genetic Algorithm (GA) Optimization. The artificial neural network (ANN) utilized in this study has a multilayer feedforward architecture comprising two hidden layers. The network is designed to accommodate four input parameters and produce a single output. The four inputs consist of several operational parameters, which encompass thermal contact resistance (TCR), gas diffusion layer (GDL) face permeability, and output voltage (V). Furthermore, the

https://doi.org/10.1021/acsomega.3c07932
ACS Omega 2024, 9, 1516−1534

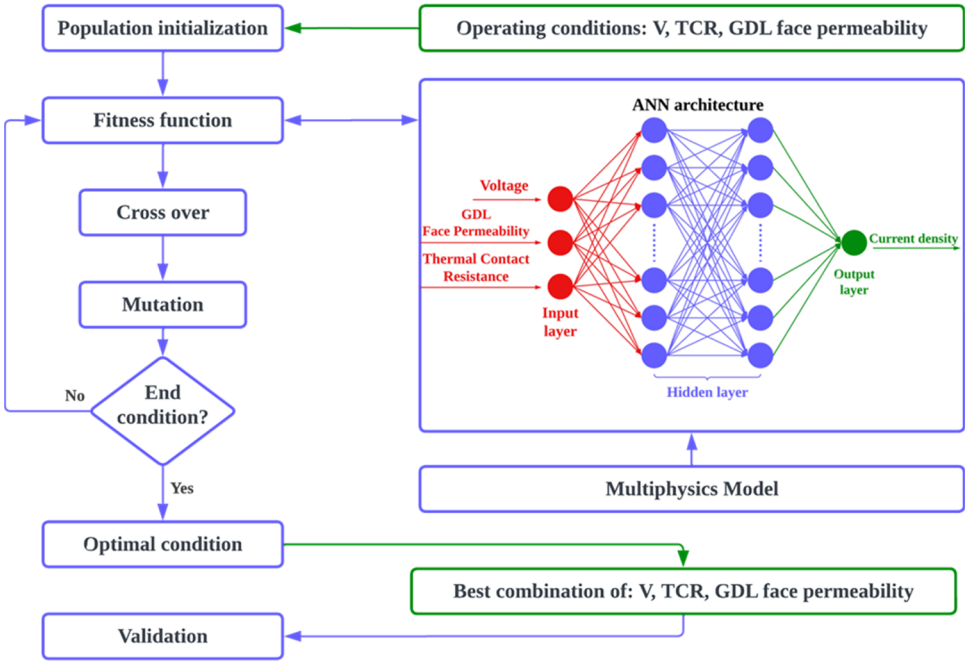

Figure 10. Combined ANN and GA optimization using 3D multiphysics simulation.

first hidden layer consists of eight neurons, whereas the second hidden layer comprises four neurons. The Levenberg–Marquardt algorithm, a training technique for feedforward networks, is chosen for its effectiveness in addressing nonlinear issues and training networks of small to medium sizes. The activation function used in the hidden layers is the hyperbolic tangent (tanh) function,[51] whereas the output layer employs the pure linear transfer function (purelin). The implicit relationship between both input and output parameters can be represented as follows

$$j = F(\text{TCR, GDL face permeability, } V) \tag{14}$$

The genetic algorithm (GA) design often incorporates several common components.[52] The essential components of this genetic algorithm framework include: (1) a set of chromosomes representing the population, (2) a fitness function used to evaluate the chromosomes, (3) the process of selecting parents from the original group of chromosomes, and (4) the application of crossover and mutation operations to generate children. The term "chromosome" is a collection of numerical parameters that serve as a representation of a potential solution for optimization using Genetic Algorithms (GA). The expression of a chromosome in n dimensions is typically represented as follows

$$\text{chromosome} = [p_1, p_2, p_3, \cdots p_i] \tag{15}$$

where p_i is the i-th parameter value. This work focuses on the consideration of four real values, namely, TCR, GDL face permeability, and V, as the elements within the ANN-GA technique. The primary objective of this optimization strategy is to maximize the power density (P). The fitness function is a metric used to identify the chromosome that possesses the ability to survive and reproduce its progeny. This function is developed by using the trained Artificial Neural Network (ANN) model.

$$P = jV = F(\text{TCR, GDL face permeability, } V) \times V \tag{16}$$

The process of selecting parent chromosomes for the purpose of reproducing the next generation is influenced by the fitness values of the chromosomes. Chromosomes that exhibit higher fitness values are more likely to be chosen for reproduction.[52] One potential manifestation of the phenomenon is the potential for chromosomes to exhibit the highest power output.

$$C(\text{TCR}_{P_{max}}, \text{GDL face permeability}_{P_{max}}, V_{P_{max}}) = \frac{P(\text{TCR}_{P_{max}}, \text{GDL face permeability}_{P_{max}}, V_{P_{max}})}{\sum_1^N P(\text{TCR, GDL face permeability, } V)} \tag{17}$$

where N is the total count of parent chromosomes, the crossover operation is a biological recombination process that involves the exchange of traits between a pair of parent chromosomes, resulting in the formation of two offspring. The mutation is typically implemented on the offspring generation's elements with a low probability in order to mitigate any potential harm to the properties of the chromosome.

The artificial neural network (ANN) and genetic algorithm (GA) are built in MATLAB using the Deep Learning Toolbox and genetic algorithm optimization toolbox (GAOT). A total of 600 data points are utilized in the training process of the artificial neural network (ANN). The selection of training, validation, and testing data points is conducted randomly, with 70% of the data points allocated for training, 15% for validation, and the remaining 15% for testing purposes. Once the artificial neural network (ANN) has been adequately trained, it functions as a fitness function for genetic algorithm (GA) optimization. The GA optimization then provides the determined operating state, in terms of current density and power, back to the ANN. The initial chromosomes in this study are generated by using a random process.

Consequently, the predictions made by the genetic algorithm (GA) may be susceptible to random mistakes. To mitigate this issue, a large number of initial chromosomes, approximately 2000, were selected. In order to minimize

https://doi.org/10.1021/acsomega.3c07932
ACS Omega 2024, 9, 1516−1534

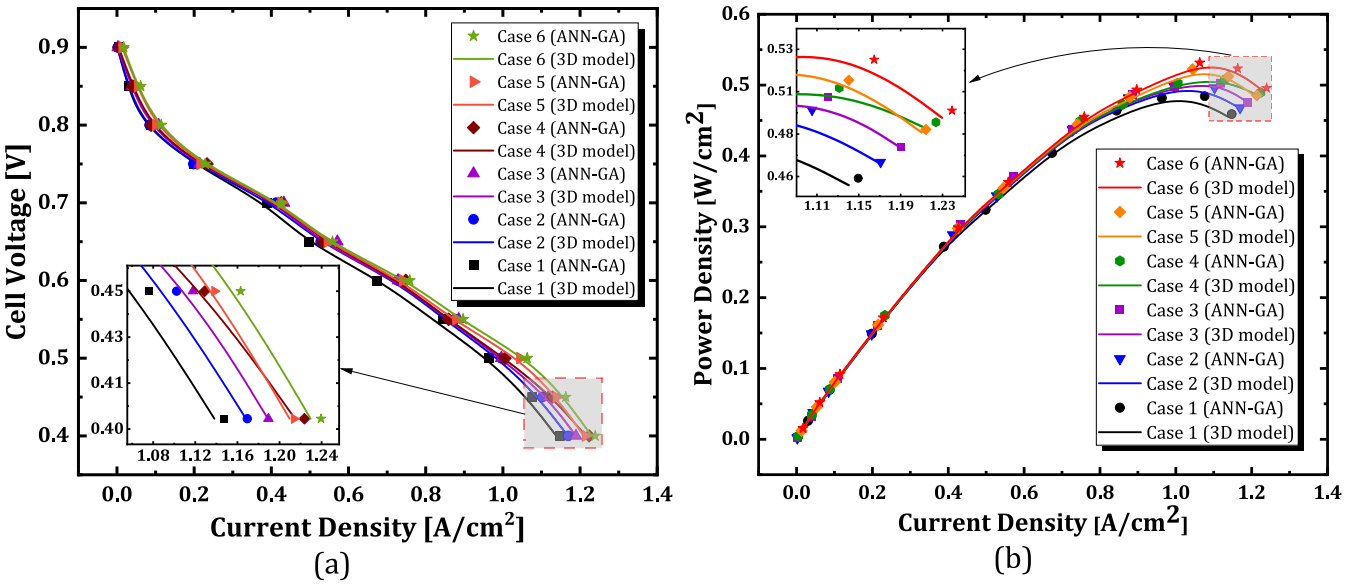

Figure 11. (a) Current density and (b) power density curves with different cases (operating pressure = 1 atm; operating temperature, T = 70 °C, O_2 mass flow rate: 2×10^{-6} kg s^{-1}, H_2 mass flow rate: 3×10^{-7} kg s^{-1}).

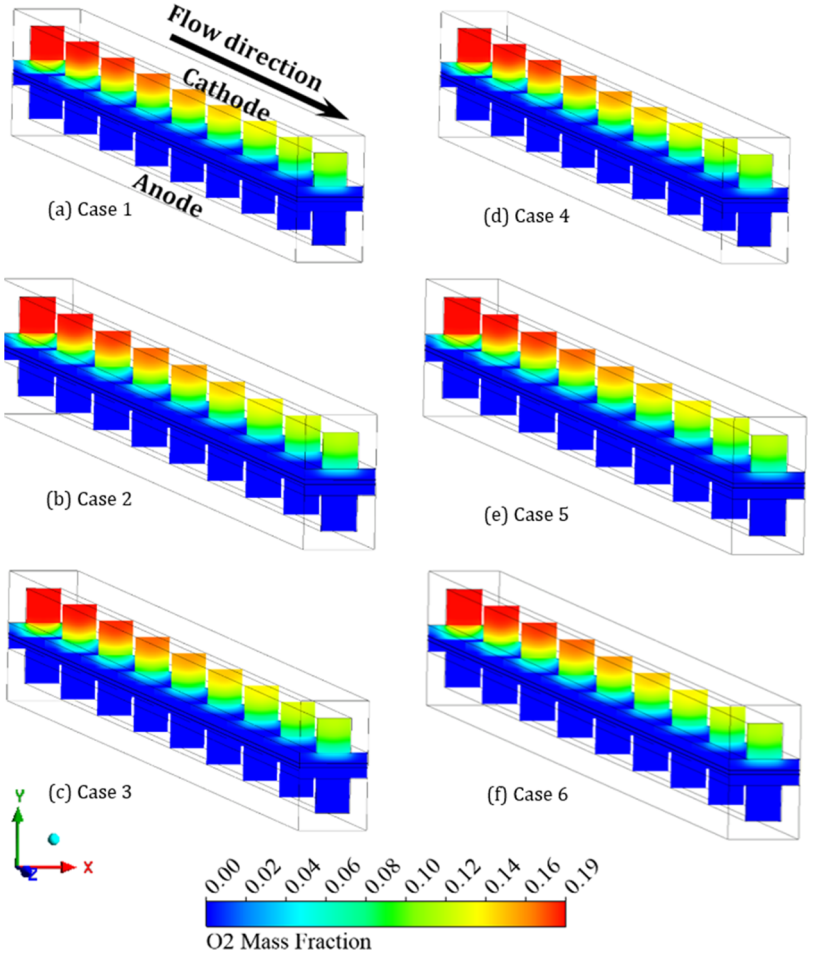

Figure 12. Contours the oxygen mass fraction in the x–y planes of the fuel cell through the z direction (gas flow) for six different cases at 0.4 V cell voltage.

computational time, the total number of evolutionary generations is established at 200. Figure 10 depicts the flowchart of the artificial neural network-genetic algorithm (ANN-GA) approach during the processes of training and prediction. Once the artificial neural network (ANN) has been adequately trained, each genetic algorithm (GA) optimization for determining the maximum power and its corresponding operating state can be completed in less than 1 s on a single

https://doi.org/10.1021/acsomega.3c07932
ACS Omega 2024, 9, 1516−1534

node. This node is equipped with an Intel (R) Core (TM) i5−7500 CPU E5−2620 3.40 GHz processor and 64 GB of RAM. This computational efficiency makes it well suited for the quick control of PEM fuel cells in practical applications.

In order to validate the results obtained using the Artificial Neural Network-Genetic Algorithm (ANN-GA) approach, the simulation results of the 3D multiphysics model are presented in Figure 11a,b. Figure 11a displays the current density curves, while Figure 11b illustrates the comparison of power density curves for six distinct scenarios, all conducted under the specified parameters. The alignment between the two forecasts is evident since it encompasses attaining the highest attainable power in both systems. The suggested artificial neural network-genetic algorithm (ANN-GA) method can offer a prompt reference for the highest achievable power and its related operating condition in an actual fuel cell system design, considering both the suitable thermal contact resistance (TCR) and gas diffusion layer (GDL) face permeability. It should be noted that the maximum power holds significant importance in various applications.

3.3. Oxygen Mass Fraction. Figure 12 illustrates the contour of oxygen mass fraction at the $x-y$ planes inside the fuel cell through the z-axis (representing gas flow) for six distinct scenarios at a cell voltage of 0.4 V. The oxygen mass fraction falls down the z-direction (cathode flow channel) within the fuel cell at the $x-y$ planes until reaching the flow channel's outflow across all examined cases. Furthermore, Figure 13 illustrates the oxygen mass fraction along the centerline of the interface between the cathode catalyst layer and the cathode gas diffusion layer within the cathode channel. This depiction pertains to six various cases and is measured at a cell voltage of 0.4 V. The oxygen mass percentage at the inlet is very similar for all examples until approximately 5 mm of channel length, after which the differences become more pronounced. Until the end of the flow channel, the oxygen mass fraction falls gradually due to oxygen consumption caused by oxygen reduction reaction (ORR) within the CCL. The findings are consistent with previous studies conducted by Zhang et al.[53] In addition, this can mean that adding GDL face permeability and TCR for all cases (excluding case 1) positively impacts the CCL's charger transfer and ORR rate increase. In contrast, the lowest O_2 mass fraction belongs to case 1, which does not consider GDL face permeability and TCR. Therefore, the oxygen mass fraction improves by 6.58% compared to case 1 (original model).

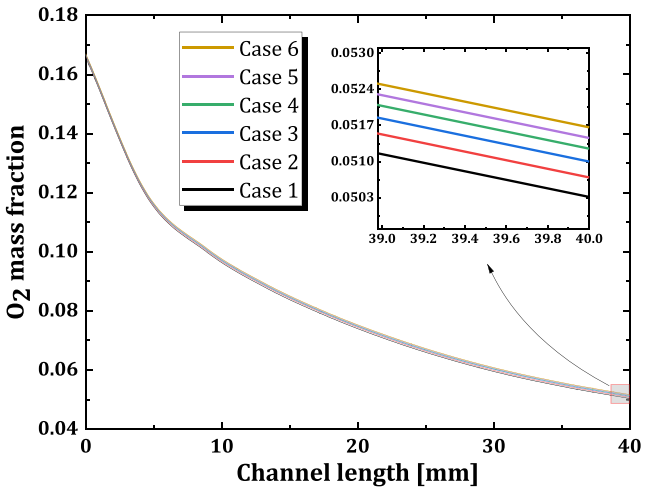

Figure 13. Mass fraction of O_2 on the centerline of the interface between CGDL and CCL examined for six different cases at 0.4 V of a cell voltage.

3.4. Hydrogen Mass Fraction. Figure 14a−f depicts the hydrogen mass fraction distribution of six cases through the anode flow channel at cell voltage 0.4 V. The hydrogen enters the anode at the bottom and exits at the bottom of the anode flow channel. It can be seen that the hydrogen mass fraction increases gradually, which means the hydrogen consumption rate for the electrochemical reaction is also increased gradually as well. In addition, Figure 15 depicts the hydrogen mass fraction along the central axis of the interface between ACL and AGDL in six distinct scenarios at 0.4 V of a cell voltage. Due to the hydrogen consumption resulting from the hydrogen oxidation reaction (HOR) within the ACL and AGDL in the regions downstream of AFC, the hydrogen mass fractions at that position typically drop gradually along the channel length (the z-direction), the trend results are similar to the preceding study.[54] At the beginning of the channel, the hydrogen mass fractions (below 0.27) show minor value differences. After that, the difference values increase dramatically due to the consumption of hydrogen, and the GDL face permeability and TCR effects are applied. Case 1 has the largest value of the hydrogen mass fraction among all cases when GDL face permeability and TCR are not included, whereas case 6 has the lowest value. This can be viewed as substantially higher GDL face permeability and TCR values being implemented to increase hydrogen consumption and decrease superfluous fuel (hydrogen) in fuel cell electrodes.

3.5. Water Mass Fraction. In comparison to the migration of water vapor, the transportation of liquid water in the gas diffusion layer (GDL) is predominantly influenced by capillary pressure and the strong adhesion of the solid skeleton to liquid water.[55] The local capillary pressure in the gas diffusion layer (GDL) can be estimated by using the Leverett-J equation, which correlates with the local water saturation. In relation to hydrophobic gas diffusion layers (GDLs), an increase in water saturation levels corresponds to an increase in the capillary pressure. This phenomenon facilitates the movement of liquid water from regions with higher saturation levels to those with lower saturation levels. Darcy's law takes into account both of these adhesion mechanisms. However, in accordance with the principle of continuity, liquid water is also susceptible to the drag exerted by the flow of gas, the impact of the water vapor phase transition, and its inherent inertia and viscosity.

Figure 16 illustrates the water mass fraction contours at the $x-y$ planes inside the fuel cell along the z-axis (representing gas flow) for six distinct scenarios at 0.4 V of cell voltage. The observed trend indicates a steady increase in the water mass fraction down the channel due to the reaction between oxygen and hydrogen at the interface between the CCL and the CGDL. Furthermore, Figure 17 depicts the mass fraction of H_2O on the central axis of the interface between CFC and CGDL throughout the cathode channel for various cases at 0.4 V of a cell voltage. The presence of water mass fraction accumulation at the interfaces of the gas diffusion layer (CGDL) and the cathode catalyst layer (CCL) in the downstream region of the flow channel can be attributed to the gas flow that occurs within the flow channel.[56] As a result of the newly introduced effect of the Forchheimer inertial coefficient for nonlinear wave motion in multiphase deformable porous media, the water mass fraction trend from the inlet

https://doi.org/10.1021/acsomega.3c07932
ACS Omega 2024, 9, 1516−1534

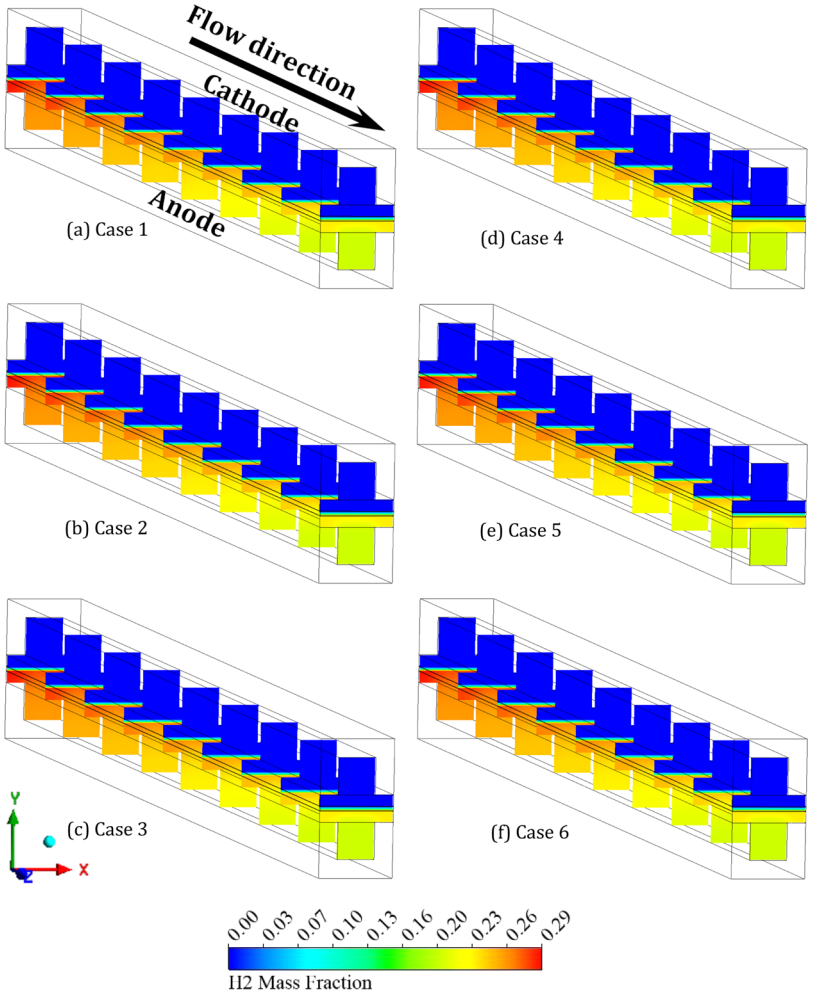

Figure 14. Contours of H_2 mass fraction at the $x-y$ planes inside the fuel cell through the z (gas flow) at 0.4 V cell voltage for six various scenarios.

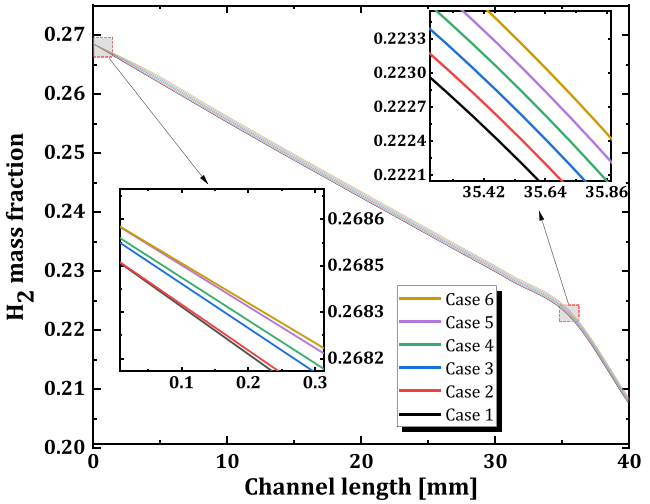

Figure 15. Mass fraction of H_2 along the centerline of the interface between the ACL and the AGDL in the anode channel at 0.4 V of cell voltage for six cases.

channel increases linearly from 0.24 to 0.29 at 5 mm channel length and then exponentially to approximately 0.38 until the end of the channel.

Considering both thermal contact resistance and GDL face permeability, it is evident that it can decrease the water mass fraction, as shown in Figure 17, where cases 2 through 6 have values lower than those of case 1. Therefore, the integration of GDL face permeability, and TCR effectively mitigates water generation. At the same time, the presence of surplus oxygen in the cathode flow channel is diminished as a result of reactant utilization in the electrochemical reaction and prevents flooding in the CGDL.

3.6. Velocity and Pressure Drops of Oxygen. This section evaluates the velocity and pressure of oxygen on the centerline of the interface between CGDL and CFC throughout the cathode channel for six cases at a cell voltage of 0.4 V, as shown in Figures 18 and 20, respectively. As shown in Figure 18, the oxygen diffusion velocity trend increases dramatically due to rising kinetic energy from the beginning of the channel until it peaks at 5 mm. The channel length is around 7.7×10^{-3} m s^{-2}; after that, it tends to remain constant and reduces due to the rate of oxygen participation in a chemical reaction, making the oxygen stay in the diffusion layer along the channel length until dropping to the end of the channel this trend can be supported by existing study.[57] In summary, the GDL face permeability and TCR for cases 2 to 6 have higher velocity values than case 1, so its performance can only be partially improved.

Figure 19 depicts the pressure profile at the $x-y$ planes inside the fuel cell throughout the z direction (flow channel) at a 0.4 V cell voltage for six cases. Due to the reduction of

https://doi.org/10.1021/acsomega.3c07932
ACS Omega 2024, 9, 1516−1534

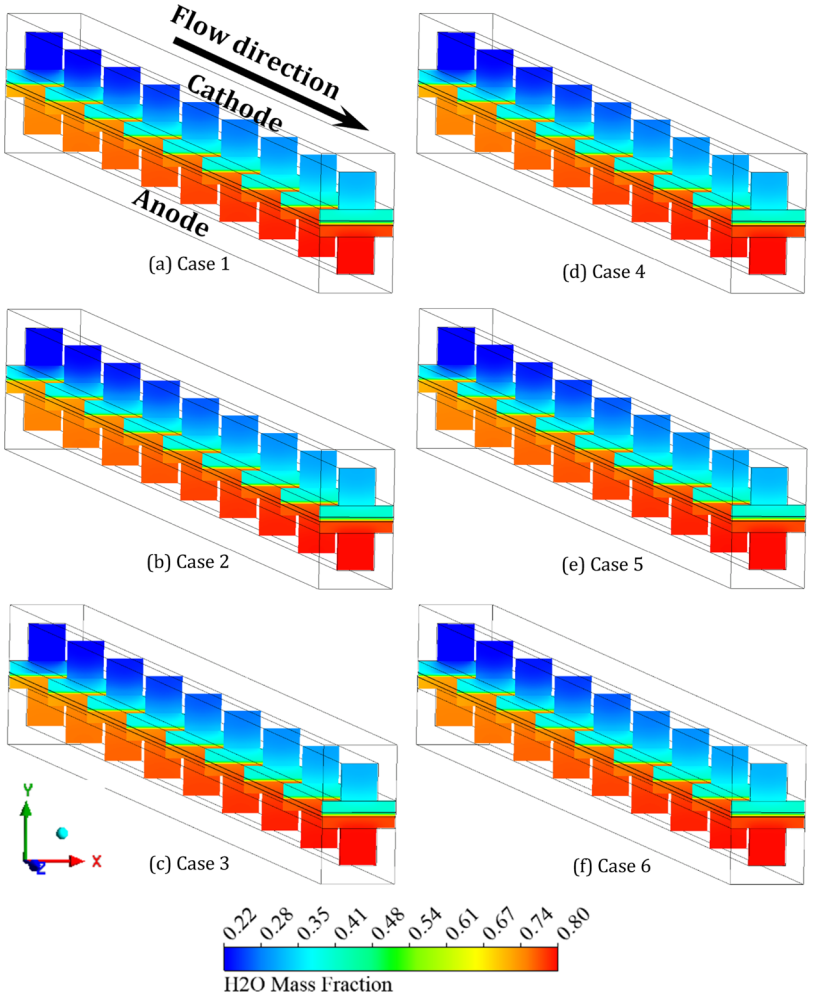

Figure 16. Contours of water mass fraction for six difference cases at the $x-y$ planes inside the fuel cell at 0.4 V cell voltage along the z (gas flow).

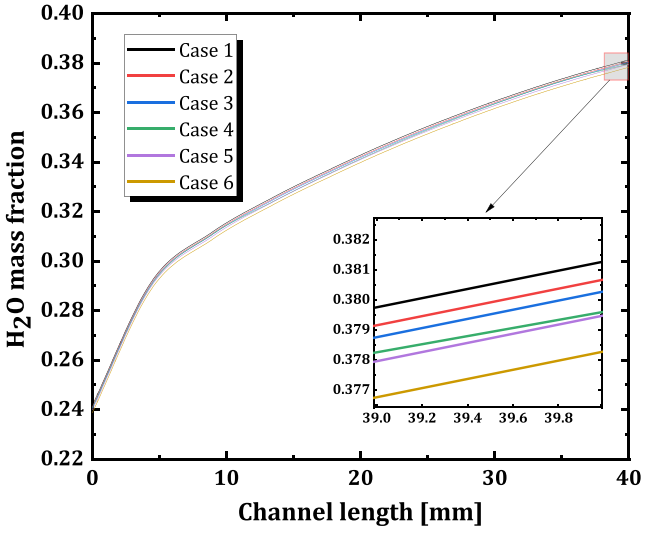

Figure 17. Mass fraction of H_2O on the centerline of the interface between CGDL and CFC across the cathode channel examined for numerous scenarios at a cell voltage of 0.4 V.

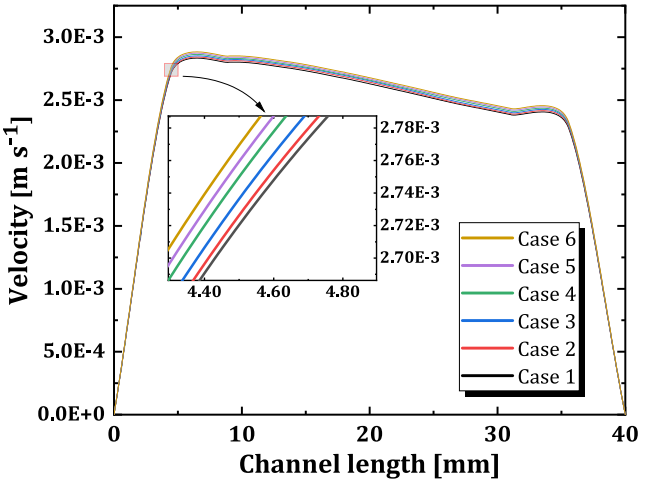

Figure 18. Velocity of oxygen at the centerline of the interface between CGDL and CFC through the cathode channel examined for different scenarios at a cell voltage of 0.4 V.

pumping work for delivering reactants to fuel cells, it is possible to detect a higher pressure near the intake CFC and CGDL that decreases gradually over the length of the channel, enhancing fuel cells' energy efficiency. In addition, Figure 20 depicts the pressure drop from approximately 55 to 13 Pa on the centerline of the interface between CGDL and CFC through the cathode channel for various scenarios at 0.4 V cell voltage. Along the channel, the pressure drop is decreasing, which is noteworthy. Meanwhile, the lowest pressure drop is observed in Case 1, which does not account for GDL face

https://doi.org/10.1021/acsomega.3c07932
ACS Omega 2024, 9, 1516−1534

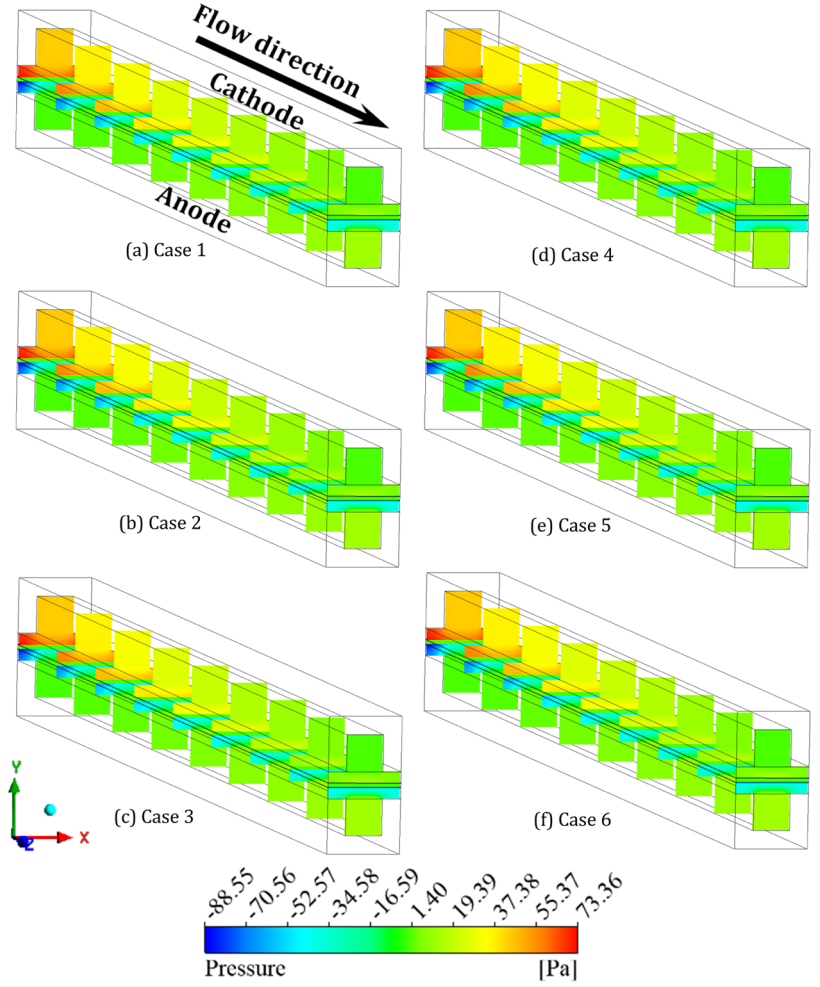

Figure 19. Pressure distributions at the $x-y$ planes inside the fuel cell through the z-axis representing gas flow examined at a cell voltage of 0.4 V for six cases.

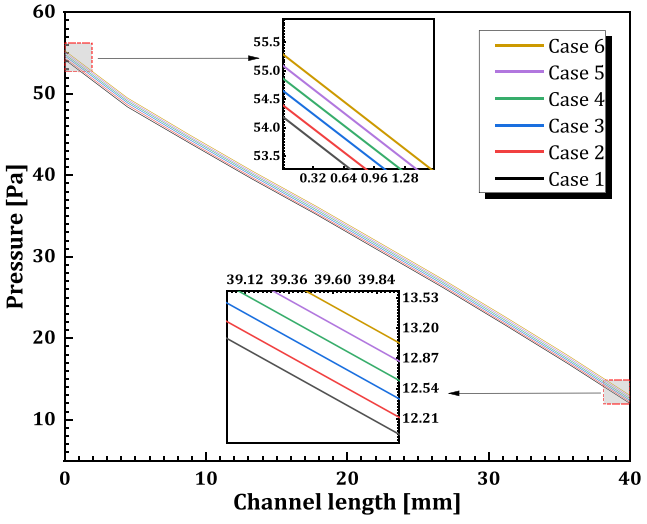

Figure 20. Pressure on the centerline of the interface between CGDL and CFC along the cathode channel examined for different scenarios at 0.4 V of a cell voltage.

permeability and TCR. To sum up, it indicates that the effect of porous medium thickness and thermal contact resistance can contribute more to the use of fuels for chemical reactions and enhance the PEM fuel cell performance.

4. CONCLUSIONS

This study employs a nonisothermal fuel cell complementary model with isotropic GDL properties to investigate the temperature profiles, mass transport, and cell performance of a PEM fuel cell under the influence of TCR and GDL face permeability on cell performances. The TCR and GDL face permeabilities of this model are determined through a comparison of the simulated temperature fluctuations between the flow plate and the cathode electrode with experimental data, resulting in a satisfactory level of agreement. The numerical model, in conjunction with the TCR and GDL face permeability, is subsequently employed to examine the effects of different methods pertaining to the TCR and GDL face permeability on the dissipation of heat and performance of a PEM fuel cell. From the computational results and discussions in the previous sections, the following conclusions can be drawn

(1) TCR and GDL face permeability influence not only the optimum temperature but also the temperature distributions of the electrode. The region adjacent to the membrane electrolyte assembly (MEA) temperature is greater than that of other parts. Taking into account the TCR and GDL face permeability results in an increase of the optimum cell temperature by approximately 1.5 °C at 0.4 V, and the temperature profiles have a "Λ" shape.

https://doi.org/10.1021/acsomega.3c07932
ACS Omega 2024, 9, 1516−1534

(2) In order to enhance the accuracy of temperature profiles and cell performance forecasts, the effects of TCR and GDL face permeability cannot be disregarded. For case 6, the proper values of TCR and GDL face permeability are determined to be 1.00×10^{-01} m^2·K/W and 3.50E12 m^{-2}, respectively. In addition, the cell performance increased by 8.72% from the original model (case 1).
(3) The influence of thermal contact resistance and appropriate GDL face permeability on velocity and oxygen mass fraction in case 6 is increased by 1.91 and 6.58%, respectively, when compared to case 1. Furthermore, case 6's pressure drop is 3.11% greater than case 1.
(4) As less energy is expended pumping reactants to fuel cells, a larger pressure can be seen near the input CFC and CGDL, and this pressure gradually drops as one moves down the channel. In addition, at 0.4 V cell voltage, the pressure along the cathode channel decreases from around 55 to 13 Pa for different cases of CFC and CGDL at the interface.
(5) The presented numerical investigations are beneficial for oxygen transport and water removal, and they enhance the uniform distribution of oxygen and current densities within fuel cells by considering the TCR and selected GDL face permeability. Further, taking the TCR and suitable GDL face permeability into account typically results in less dissolved water in the cathode catalyst layer, leading to better cell performance.
(6) In addition, the ANN-GA technique was utilized to determine the optimal power densities that can be achieved in six distinct scenarios. These findings hold significance for designing and efficiently monitoring fuel cell systems.

In conclusion, the research results offer valuable insights into how TCR and GDL face permeability affect temperature profiles and the performance of PEMFCs. The suitable TCR and GDL face permeability values for a single PEMFC can vary depending on several factors, including the fuel cell's design, operating conditions, and materials utilized for further study.

AUTHOR INFORMATION

Corresponding Author

Ocktaeck Lim − *School of Mechanical Engineering, University of Ulsan, Ulsan 44610, South Korea;* orcid.org/0000-0001-8130-0838; Email: otlim@ulsan.ac.kr

Author

Binyamin Binyamin − *Graduate School of Mechanical Engineering, University of Ulsan, Ulsan 44610, South Korea; Department of Mechanical Engineering, Universitas Muhammadiyah Kalimantan Timur, Samarinda 75124, Indonesia*

Complete contact information is available at: https://pubs.acs.org/10.1021/acsomega.3c07932

Author Contributions

B.B.: conceptualization, original draft writing, methodology, investigation, data curation, formal analysis. O.L.: funding acquisition, supervision, project administration, review, and editing.

Notes

The authors declare no competing financial interest.

ACKNOWLEDGMENTS

This results was supported by "Regional Innovation Strategy (RIS)" through the National Research Foundation of Korea (NRF) funded by the Ministry of Education (MOE) (2021RIS-003). This work was supported by the Technology Innovation Program (or Industrial Strategic Technology Development Program-The Safety Based Technology Development and Substantiation of Small Hydrogen Powered Vessel) (RS-2022-00142947, The technology development on fuel cell electric propulsion system using Land Based Test Site) funded By the Ministry of Trade, Industry & Energy (MOTIE, Korea). This work was supported by Regional Innovation Cluster Development (R&D) by the Ministry of Trade, Industry and Energy (MOTIE, Korea) [Project Name: Open Innovation Project for Convergence Industry of Battery/Fuel Cell for Mobility Electrification and Energy Production/Storage (P0025406)]. This work was supported by the National Research Foundation of Korea (NRF) grant funded by the Korea government (MSIT) (No. RS-2023-00217778).

NOMENCLATURE

Abbreviation

ABP	anode bipolar plate
ACL	anode catalyst layer
AGDL	anode gas diffusion layer
AFC	anode flow channel
CBP	cathode bipolar plate
CCL	cathode catalyst layer
CGDL	cathode gas diffusion layer
CFC	cathode flow channel
HTC	coefficient of heat transfer
MEA	membrane electrode assembly
PEMFC	proton exchange membrane fuel cell
TCR	thermal contact resistance
a	water activity
A	area, m^{-2}
A_s	specific area of catalyst layer, m^{-1}
D	coefficient of diffusion, m^2 s^{-1}
F	Faraday constant, 96,485 C mol^{-1}
h	coefficient of heat transfer
k	conductivity of thermal, W m^{-1} K^{-1}
K	hydraulic permeability, m^2
RH	relative humidity
s	liquid water saturation
T	temperature, K
V	voltage, V
W	width, mm
Y	fraction of mass
α	coefficient of transfer
ε	porosity
ϕ	potential, V
η	overpotential, V
λ	membrane water content
σ	electric conductivity, S m^{-1}
ζ	stoichiometric flow ratio

Subscripts and superscripts

a	anode
c	cathode, capillary
ch	channel dissolved
e	State of equilibrium
eff	effective
g	gas phase

https://doi.org/10.1021/acsomega.3c07932
ACS Omega 2024, 9, 1516−1534

h	hydrogen
k	species
l	liquid
mem	membrane
O	oxygen
OC	open circuit
ref	reference
rib	rib
sat	saturation

REFERENCES

(1) Li, H.-W.; Xu, B.; Du, C.; Yang, Y. Performance Prediction and Power Density Maximization of a Proton Exchange Membrane Fuel Cell Based on Deep Belief Network. *J. Power Sources* **2020**, *461*, No. 228154.

(2) Zhou, D.; Al-durra, A.; Gao, F.; Ravey, A.; Matraji, I.; Godoy, M. Online Energy Management Strategy of Fuel Cell Hybrid Electric Vehicles Based on Data Fusion Approach. *J. Power Sources* **2017**, *366*, 278−291, DOI: 10.1016/j.jpowsour.2017.08.107.

(3) Stempien, J. P.; Chan, S. H. Comparative Study of Fuel Cell, Battery and Hybrid Buses for Renewable Energy Constrained Areas. *J. Power Sources* **2017**, *340*, 347−355.

(4) Kosakian, A.; Urbina, L. P.; Heaman, A.; Secanell, M. Electrochimica Acta Understanding Single-Phase Water-Management Signatures in Fuel- Cell Impedance Spectra : A Numerical Study. *Electrochim. Acta* **2020**, *350*, No. 136204.

(5) Ding, Y.; Xu, L.; Zheng, W.; Hu, Z.; Shao, Y.; Li, J.; Ouyang, M. Characterizing the Two-Phase Flow Effect in Gas Channel of Proton Exchange Membrane Fuel Cell with Dimensionless Number. *Int. J. Hydrogen Energy* **2023**, *48* (13), 5250−5265.

(6) Xu, C.; Wang, H.; Cheng, T. Wave-Shaped Flow Channel Design and Optimization of PEMFCs with a Groove in the Gas Diffusion Layer. *Int. J. Hydrogen Energy* **2023**, *48* (11), 4418−4429.

(7) Yang, X.; Meng, X.; Sun, J.; Song, W.; Sun, S.; Shao, Z. Study on Internal Dynamic Response during Cold Start of Proton Exchange Membrane Fuel Cell with Parallel and Serpentine Flow Fields. *J. Power Sources* **2023**, *561*, No. 232609.

(8) Wang, Q.; Tang, F.; Li, B.; Dai, H.; Zheng, J. P.; Zhang, C.; Ming, P. Numerical Analysis of Static and Dynamic Heat Transfer Behaviors inside Proton Exchange Membrane Fuel Cell. *J. Power Sources* **2021**, *488*, No. 229419.

(9) Ge, N.; Chevalier, S.; Lee, J.; Yip, R.; Banerjee, R.; George, M. G.; Liu, H.; Lee, C.; Fazeli, M.; Antonacci, P.; Kotaka, T.; Tabuchi, Y.; Bazylak, A. International Journal of Heat and Mass Transfer Non-Isothermal Two-Phase Transport in a Polymer Electrolyte Membrane Fuel Cell with Crack-Free Microporous Layers. *Int. J. Heat Mass Transfer* **2017**, *107*, 418−431.

(10) Xing, L.; Du, S.; Chen, R.; Mamlouk, M.; Scott, K. Anode Partial Fl Ooding Modelling of Proton Exchange Membrane Fuel Cells: Model Development and Validation. *Energy* **2016**, *96*, 80−95.

(11) Bhaiya, M.; Putz, A.; Secanell, M. Electrochimica Acta Analysis of Non-Isothermal Effects on Polymer Electrolyte Fuel Cell Electrode Assemblies. *Electrochim. Acta* **2014**, *147*, 294−309.

(12) Song, J.; Huang, Y.; Zeng, J.; Chen, L.; Wu, Y. Design and Numerical Investigation of Multi-Channel Cooling Plate for Proton Exchange Membrane Fuel Cell. *Energy Rep.* **2022**, *8*, 6058−6067.

(13) Cao, T.; Mu, Y.; Ding, J.; Lin, H.; He, Y.; Tao, W. International Journal of Heat and Mass Transfer Modeling the Temperature Distribution and Performance of a PEM Fuel Cell with Thermal Contact Resistance. *Int. J. Heat Mass Transfer* **2015**, *87*, 544−556.

(14) Islam, S. In *Modeling and Control of Fuel Cell Power System with Varying Load and Temperature*, 2020 IEEE/ASME International Conference on Advanced Intelligent Mechatronics (AIM); IEEE, 2020; pp 1236−1241.

(15) Goshtasbi, A.; Pence, B. L.; Ersal, T. Computationally Efficient Pseudo-2D Non-Isothermal Modeling of Polymer Electrolyte Membrane Fuel Cells with Two-Phase Phenomena. *J. Electrochem. Soc.* **2016**, *163* (13), 24−26, DOI: 10.1149/2.0871613jes.

(16) Burheim, O. S.; Pollet, B. G. Thermal Gradients and Thermal Conductivity in PEM Fuel Cells, Compared to Li-Ion Batteries and Super Capacitors. *ECS Trans.* **2018**, *86* (13), No. 97, DOI: 10.1149/08613.0097ecst.

(17) Wang, H.-N.; Zhu, X.; Liao, Q.; Chen, R.; Ye, D.; Sui, P. C.; Djilali, N. Numerical Simulation on Mass Transport in a Passive Vapor-Fed Direct Methanol Fuel Cell Operating with Neat Methanol. *J. Power Sources* **2020**, *477*, No. 228541.

(18) Binyamin; Lim, O. Numerical Investigation of Tapered Flow Field Configuration to Improve Mass Transport and Performance of Proton Exchange Membrane Fuel Cell. *Int. J. Hydrogen Energy* **2023**, *50*, 470−491, DOI: 10.1016/j.ijhydene.2023.08.247.

(19) Bapat, C. J.; Thynell, S. T. Anisotropic Heat Conduction Effects in Proton-Exchange Membrane Fuel Cells. *J. Heat Transfer* **2007**, *129* (9), 1109−1118.

(20) Nitta, I.; Himanen, O.; Mikkola, M. Thermal Conductivity and Contact Resistance of Compressed Gas Diffusion Layer of PEM Fuel Cell. *Fuel Cells* **2008**, *8* (2), 111−119.

(21) Sadeghi, E.; Djilali, N.; Bahrami, M. Effective Thermal Conductivity and Thermal Contact Resistance of Gas Diffusion Layers in Proton Exchange Membrane Fuel Cells. Part 1: Effect of Compressive Load. *J. Power Sources* **2011**, *196* (1), 246−254.

(22) Zhao, J.; Tu, Z.; Chan, S. H. Carbon Corrosion Mechanism and Mitigation Strategies in a Proton Exchange Membrane Fuel Cell (PEMFC): A Review. *J. Power Sources* **2021**, *488*, No. 229434.

(23) Zhao, J.; Li, S.; Tu, Z. Development of Practical Empirically and Statistically-Based Equations for Predicting the Temperature Characteristics of PEMFC Applied in the CCHP System. *Int. J. Hydrogen Energy* **2023**. DOI: 10.1016/j.ijhydene.2022.12.180.

(24) Zhao, J.; Zhou, C.; Han, J.; Chen, K.; Ren, Y. Numerical Analysis of Improved Water Management of Open-Cathode Proton Exchange Membrane Fuel Cells with a Dead-Ended Anode by Pulsating Flow. *Int. J. Hydrogen Energy* **2023**, *48*, 16858−16874, DOI: 10.1016/j.ijhydene.2023.01.118.

(25) Shang, K.; Han, C.; Jiang, T.; Chen, Z. Numerical Study of PEMFC Heat and Mass Transfer Characteristics Based on Roughness Interface Thermal Resistance Model. *Int. J. Hydrogen Energy* **2023**, *48* (20), 7460−7475.

(26) Liu, Q.; Lan, F.; Chen, J.; Wang, J.; Zeng, C. Effect of Anisotropic Transport Properties of Porous Layers on the Dynamic Performance of Proton Exchange Membrane Fuel Cell. *Int. J. Hydrogen Energy* **2023**, *48* (29), 10982−11002.

(27) Wan, Z.; Yan, H.; Sun, Y.; Yang, C.; Chen, X.; Kong, X.; Chen, Y.; Tu, Z.; Wang, X. Thermal Management Improvement of Air-Cooled Proton Exchange Membrane Fuel Cell by Using Metal Foam Flow Field. *Appl. Energy* **2023**, *333*, No. 120642.

(28) Martín-Alcántara, A.; Pino, J.; Iranzo, A. New Insights into the Temperature-Water Transport-Performance Relationship in PEM Fuel Cells. *Int. J. Hydrogen Energy* **2023**, *48*, 13987−13999, DOI: 10.1016/j.ijhydene.2022.12.281.

(29) Wang, J.; Wang, S.; Zhu, Y.; Wang, Y. Effect of Cooling Surface Temperature Difference on the Performance of High-Temperature PEMFCs. *Int. J. Hydrogen Energy* **2023**, *48*, 16813−16828, DOI: 10.1016/j.ijhydene.2023.01.125.

(30) Yao, J.; Wu, Z.; Wang, H.; Yang, F.; Xuan, J.; Xing, L.; Ren, J.; Zhang, Z. Design and Multi-Objective Optimization of Low-Temperature Proton Exchange Membrane Fuel Cells with Efficient Water Recovery and High Electrochemical Performance. *Appl. Energy* **2022**, *324*, No. 119667, DOI: 10.1016/j.apenergy.2022.119667.

(31) Xu, C.; Wang, H.; Cheng, T. Study on the Net Power Density Improvement of Staggered Trapezoidal Baffle Flow Channel for PEMFC. *Ionics* **2023**, *29*, 4775−4785, DOI: 10.1007/s11581-023-05198-2.

(32) Xu, C.; Wang, H.; Li, Z.; Cheng, T. Effects of the Design and Optimization of Trapezoidal Channels and Baffles (Number and Position) on the Net Power Density of Proton-Exchange Membrane Fuel Cells. *ACS Omega* **2022**, *7* (5), 4214−4223.

https://doi.org/10.1021/acsomega.3c07932
ACS Omega 2024, 9, 1516−1534

(33) Pang, Y.; Wang, Y. Water Spatial Distribution in Polymer Electrolyte Membrane Fuel Cell: Convolutional Neural Network Analysis of Neutron Radiography. *Energy AI* **2023**, *14*, No. 100265.
(34) Wang, J.; Jiang, H.; Chen, G.; Wang, H.; Lu, L.; Liu, J.; Xing, L. Integration of Multiphysics and Machine Learning-Based Surrogate Modelling Approaches for Multi-Objective Optimization of Deformed GDL of PEM Fuel Cells. *Energy AI* **2023**, *14*, No. 100261.
(35) Wang, L.; Husar, A.; Zhou, T.; Liu, H. A Parametric Study of PEM Fuel Cell Performances. *Int. J. Hydrogen Energy* **2003**, *28* (11), 1263−1272.
(36) Min, C. H.; He, Y. L.; Liu, X. L.; Yin, B. H.; Jiang, W.; Tao, W. Q. Parameter Sensitivity Examination and Discussion of PEM Fuel Cell Simulation Model Validation. Part II: Results of Sensitivity Analysis and Validation of the Model. *J. Power Sources* **2006**, *160* (1), 374−385.
(37) Tao, W. Q.; Min, C. H.; Liu, X. L.; He, Y. L.; Yin, B. H.; Jiang, W. Parameter Sensitivity Examination and Discussion of PEM Fuel Cell Simulation Model Validation. Part I. Current Status of Modeling Research and Model Development. *J. Power Sources* **2006**, *160* (1), 359−373.
(38) Patankar, S. V.*Numerical Heat Transfer and Fluid Flow*; CRC Press: Boca Raton, 2018.
(39) Berning, T.; Lu, D. M.; Djilali, N. Three-Dimensional Computational Analysis of Transport Phenomena in a PEM Fuel Cell. *J. Power Sources* **2002**, *106* (1−2), 284−294.
(40) Zamel, N.; Li, X.; Shen, J. Correlation for the Effective Gas Diffusion Coefficient in Carbon Paper Diffusion Media. *Energy Fuels* **2009**, *23* (12), 6070−6078.
(41) Tomadakis, M. M.; Robertson, T. J. Viscous Permeability of Random Fiber Structures: Comparison of Electrical and Diffusional Estimates with Experimental and Analytical Results. *J. Compos. Mater.* **2005**, *39* (2), 163−188, DOI: 10.1177/0021998305046438.
(42) Zamel, N.; Li, X.; Shen, J.; Becker, J.; Wiegmann, A. Estimating Effective Thermal Conductivity in Carbon Paper Diffusion Media. *Chem. Eng. Sci.* **2010**, *65* (13), 3994−4006.
(43) Liu, X.; Tao, W.; Li, Z.; He, Y. Three-Dimensional Transport Model of PEM Fuel Cell with Straight Flow Channels. *J. Power Sources* **2006**, *158*, 25−35.
(44) Springer, T. E.; Zawodzinski, T. A.; Gottesfeld, S. Polymer Electrolyte Fuel Cell Model. *J. Electrochem. Soc.* **1991**, *138* (8), 2334−2342.
(45) Wang, Y.; Wang, C.-Y. A Nonisothermal, Two-Phase Model for Polymer Electrolyte Fuel Cells. *J. Electrochem. Soc.* **2006**, *153* (6), No. A1193, DOI: 10.1149/1.2193403.
(46) Ye, Q.; Van Nguyen, T. Three-Dimensional Simulation of Liquid Water Distribution in a PEMFC with Experimentally Measured Capillary Functions. *J. Electrochem. Soc.* **2007**, *154* (12), No. B1242, DOI: 10.1149/1.2783775.
(47) Cao, T. F.; Lin, H.; Chen, L.; He, Y. L.; Tao, W. Q. Numerical Investigation of the Coupled Water and Thermal Management in PEM Fuel Cell. *Appl. Energy* **2013**, *112*, 1115−1125.
(48) Binyamin, B.; Lim, O. Numerical Analysis of the Structural and Flow Rate Characteristics of the Fuel Injection Pump in a Marine Diesel Engine. *Sustainability* **2023**, *15* (11), No. 8948, DOI: 10.3390/su15118948.
(49) Xia, L.; Zhang, C.; Hu, M.; Jiang, S.; Chin, C. S.; Gao, Z.; Liao, Q. Investigation of Parameter Effects on the Performance of High-Temperature PEM Fuel Cell. *Int. J. Hydrogen Energy* **2018**, *43* (52), 23441−23449.
(50) Sadeghifar, H.; Djilali, N.; Bahrami, M. Effect of Polytetrafluoroethylene (PTFE) and Micro Porous Layer (MPL) on Thermal Conductivity of Fuel Cell Gas Diffusion Layers: Modeling and Experiments. *J. Power Sources* **2014**, *248*, 632−641.
(51) Kizilkan, Z. B.; Sivri, M. S.; Yazici, I.; Beyca, O. F.Neural Networks and Deep Learning. In *Business Analytics for Professionals*; Springer, 2022; pp 127−151.
(52) Haupt, S. E.Introduction to Genetic Algorithms. In *Artificial Intelligence Methods in the Environmental Sciences*; Springer, 2009; pp 103−125.
(53) Zhang, Y.; He, S.; Jiang, X.; Xiong, M.; Ye, Y.; Yang, X. Three-Dimensional Multiphase Simulation of Proton Exchange Membrane Fuel Cell Performance Considering Constriction Straight Channel. *Energy* **2023**, *267*, No. 126544.
(54) Rostami, L.; Haghshenasfard, M.; Sadeghi, M.; Zhiani, M. A 3D CFD Model of Novel Flow Channel Designs Based on the Serpentine and the Parallel Design for Performance Enhancement of PEMFC. *Energy* **2022**, *258*, No. 124726.
(55) Nam, J. H.; Kaviany, M. Effective Diffusivity and Water-Saturation Distribution in Single- and Two-Layer PEMFC Diffusion Medium. *Int. J. Heat Mass Transfer* **2003**, *46* (24), 4595−4611.
(56) Chen, B.; Liu, Q.; Zhang, C.; Liu, Y.; Shen, J.; Tu, Z. Numerical Study on Water Transfer Characteristics under Joint Effect of Placement Orientation and Flow Channel Size for PEMFC with Dead-Ended Anode. *Energy* **2022**, *254*, No. 124365, DOI: 10.1016/j.energy.2022.124365.
(57) Li, H. W.; Liu, J. N.; Yang, Y.; Fan, W.; Lu, G. L. Research on Mass Transport Characteristics and Net Power Performance under Different Flow Channel Streamlined Imitated Water-Drop Block Arrangements for Proton Exchange Membrane Fuel Cell. *Energy* **2022**, *251*, No. 123983, DOI: 10.1016/j.energy.2022.123983.

https://doi.org/10.1021/acsomega.3c07932
ACS Omega 2024, 9, 1516−1534